A&A 674, A8 (2023)
https://doi.org/10.1051/0004-6361/202243809

Astronomy & Astrophysics
Special issue

Gaia Data Release 3

Gaia Data Release 3

Properties of the line-broadening parameter derived with the Radial Velocity Spectrometer (RVS)

Y. Frémat[1,⋆], F. Royer[2,⋆], O. Marchal[3], R. Blomme[1], P. Sartoretti[2], A. Guerrier[4], P. Panuzzo[2], D. Katz[2], G. M. Seabroke[5], F. Thévenin[6], M. Cropper[5], K. Benson[5], Y. Damerdji[7,8], R. Haigron[2], A. Lobel[1], M. Smith[5], S. G. Baker[5], L. Chemin[9], M. David[10], C. Dolding[5], E. Gosset[8,11], K. Janßen[12], G. Jasniewicz[13], G. Plum[2], N. Samaras[1,14], O. Snaith[2], C. Soubiran[15], O. Vanel[2], J. Zorec[16], T. Zwitter[17], N. Brouillet[15], E. Caffau[2], F. Crifo[2], C. Fabre[4], F. Fragkoudi[18,19], H. E. Huckle[5], Y. Lasne[4], N. Leclerc[2], A. Mastrobuono-Battisti[2], A. Jean-Antoine Piccolo[4], and Y. Viala[2]

(Affiliations can be found after the references)

Received 19 April 2022 / Accepted 23 June 2022

ABSTRACT

Context. The third release of the *Gaia* catalogue contains radial velocities for 33 812 183 stars with effective temperatures ranging from 3100 K to 14 500 K. The measurements are based on the comparison of the spectra observed with the Radial Velocity Spectrometer (RVS; wavelength coverage: 846–870 nm, median resolving power: 11 500) to synthetic data broadened to the adequate along-scan line spread function. The additional line-broadening, fitted as it would only be due to axial rotation, is also produced by the pipeline and is available in the catalogue (field name `vbroad`).

Aims. We describe the properties of the line-broadening information extracted from the RVS and published in the catalogue, and analyse the limitations imposed by the adopted method, wavelength range, and instrument.

Methods. We used simulations to express the link between the line-broadening measurement provided in *Gaia* Data Release 3 and $V \sin i$. We then compared the observed values to the measurements published by various catalogues and surveys (GALAH, APOGEE, LAMOST, etc.).

Results. While we recommend caution in the interpretation of the `vbroad` measurement, we also find a reasonable general agreement of the *Gaia* Data Release 3 line-broadening values and values in other catalogues. We discuss and establish the validity domain of the published `vbroad` values. The estimate tends to be overestimated at the lower $V \sin i$ end, and at $T_{\rm eff} > 7500$ K its quality and significance degrade rapidly when $G_{\rm RVS} > 10$. Despite all the known and reported limitations, the *Gaia* Data Release 3 line-broadening catalogue contains measurements obtained for 3 524 677 stars with $T_{\rm eff}$ ranging from 3500 to 14 500 K, and $G_{\rm RVS} < 12$. It gathers the largest stellar sample ever considered for the purpose, and allows a first mapping of the *Gaia* line-broadening parameter across the Hertzsprung-Russel diagram.

Key words. stars: rotation – catalogs

1. Introduction

In addition to its high-quality astrometry, the ESA *Gaia* space mission provides valuable spectroscopic data. The satellite carries a spectrometer with intermediate resolving power that covers the 846 to 870 nm wavelength range, with the initial primary goal of measuring the radial velocity (RV) of the sources transiting one of its four CCD rows (Sartoretti et al. 2022; Cropper et al. 2018) down to the magnitude $G_{\rm RVS} = 16.2$ (Katz et al. 2023). During one such transit, the instrument acquires three spectra (i.e. one per CCD strip) in ∼4.4 s each. A spectroscopic pipeline processes the data (Sartoretti et al. 2018) to calibrate and extract the transit spectra, then derives the RV and a line-broadening parameter through the single-transit analysis (STA) and multiple-transit analysis chains (MTA). The third release of the *Gaia* catalogue contains the radial velocity of 33 812 183 stars with effective temperatures ranging from 3100 to 14 500 K. Its measurement is based on the comparison of observed spectra to synthetic template spectra (David et al. 2014) and assumes that the central wavelength, strength, and shape of the observed spectral lines are accurately known. Various physical phenomena can contribute to broadening or shifting the intrinsic profile of spectral lines. They relate to quantum mechanics, particle interaction, or to motions with velocity fields on scales shorter than the mean free path of the photons. In most cases, the magnitude of their impact on the spectra is well described by classical atmosphere modelling, and the spectral line shapes can usually be predicted by keeping the effective temperature, surface gravity, metallicity, and microturbulence fixed. The adopted method therefore relies on a set of synthetic spectrum libraries covering the astrophysical parameter (APs) space ($T_{\rm eff}$, $\log g$, and [M/H]) and on the knowledge of the stellar APs (Katz et al. 2023; Blomme et al. 2023; Damerdji et al., in prep.).

For most targets, the line-broadening at the median resolving power of the RVS ($R = 11\,500$, ∼26 km s^{-1}, Cropper et al. 2018) is expected to be dominated by the instrumental spectroscopic line spread function (along-scan line spread function, henceforth LSF; Sartoretti et al. 2022). There are other mechanisms, however, that may also significantly broaden the lines and that require the measurement of additional parameters. The most significant of these is stellar axial rotation, whose line-broadening is due to the Doppler effect and depends on the equatorial rotational velocity, V, and on the stellar inclination angle, i.

Rotational broadening leads to line blending and hence to complex template mismatches that impact the RV

⋆ Corresponding authors: Y. Frémat,
e-mail: `yves.fremat@observatory.be`;
F. Royer, e-mail: `frederic.royer@obspm.fr`

measurements. A first attempt to derive $V \sin i$ was therefore included in the STA and MTA chains (Sartoretti et al. 2018, 2022). On the other hand, it is known that phenomena other than stellar rotation may contribute to broadening the spectroscopic features (e.g. macroscopic random motions such as macro-turbulence, $V_{\rm macro}$, and large convection eddies, prominences, radial and non-radial pulsations, systematic velocity fields related to stellar winds, ignored binarity, or the limited accuracy of the LSF or of the straylight correction). We did not try to disentangle their impact on the line profiles from the rotational broadening, and ignored them when we estimated $V \sin i$ (e.g. the synthetic spectra we adopted assume $V_{\rm macro} = 0\,{\rm km\,s^{-1}}$).

Therefore, while the line-broadening is measured with a classic rotational kernel, the measurement provided in the catalogue is called `vbroad`. For the same reason, `vbroad` refers to the estimate provided by the STA/MTA parts of the spectroscopic pipeline throughout, while $V \sin i$ denotes the true projected rotational velocity value (e.g. from simulations) or the value found in other catalogues or surveys (i.e. even when the catalogue or survey itself does not distinguish $V \sin i$ from other broadening mechanisms, and/or similarly calls the estimate by a different name).

Another estimate of the RVS line-broadening is obtained by the ESP-HS[1] module of the Apsis[2] pipeline (Creevey et al. 2023). It is published in *Gaia* DR3 as `vsini_esphs` (in the `astrophysical_parameters` table) and is an intermediate result of the analysis of the RVS and BP/RP data when the astrophysical parameters of stars with $T_{\rm eff} > 7500\,K$ are derived. A discussion of `vsini_esphs` and a comparison with the `vbroad` measurements described in the present paper is given in the online documentation (Sect. 11.4.4, Korn et al. 2022) and in Fouesneau et al. (2023). In this work, we provide more information about the line-broadening parameter for the *Gaia* DR3 catalogue user as it is derived from the spectra obtained by the *Gaia* Radial Velocity Spectrometer (RVS) and derived by the spectroscopic pipeline. The adopted method to derive it together with the expected accuracy, limitations, and significance is described in Sect. 2. We provide a general overview of the results in Sect. 3. During the validation process, the pipeline output was compared to values found in various catalogues. We report our findings in Sect. 4 and discuss the statistical behaviour, offsets, and dispersion in Sect. 5. Our main conclusions are summarised in Sect. 6.

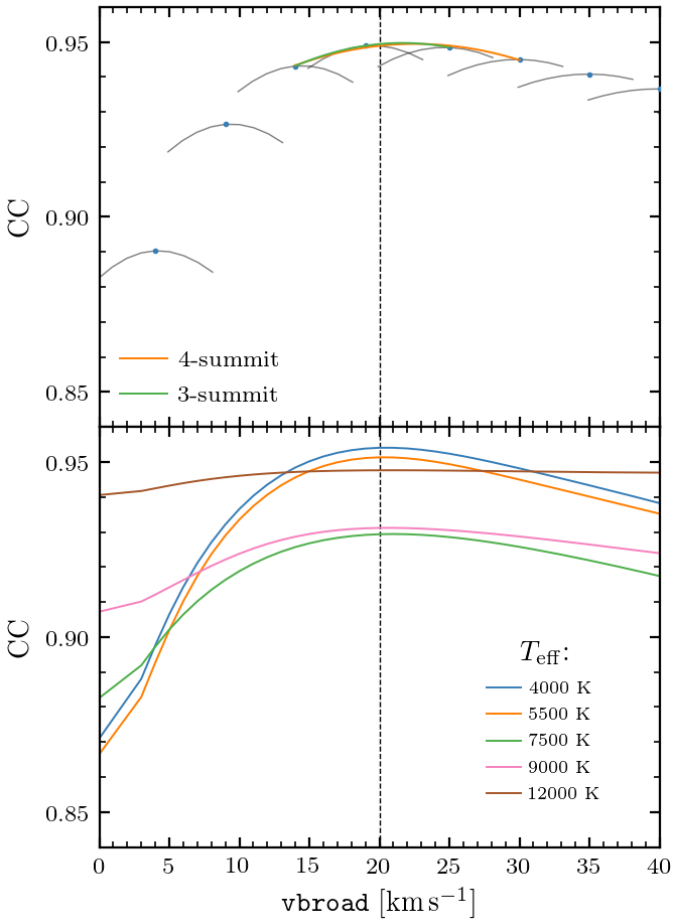

Fig. 1. `vbroad` determination at $T_{\rm eff} = 5500\,{\rm K}$, $\log g = 4.5$, [Fe/H] = 0, `vbroad` $= 20\,{\rm km\,s^{-1}}$ (vertical dashed line), and $G_{\rm RVS} = 8$. Template mismatch errors are ignored, except for the `vbroad` broadening, which is the quantity to be derived. *Upper panel*: top of the CCF centred at $0\,{\rm km\,s^{-1}}$ (grey curves) obtained by assuming various values of `vbroad` is plotted and shifted according to the adopted `vbroad`. The peaks are identified by blue circles, and the three-peak and four-peak parabola fits are shown by green and orange curves, respectively. The ordinate axis label 'CC' stands for 'cross-correlation coefficient'. *Lower panel*: same as in the upper panel, but at different effective temperature values. For clarity, the CCF peaks are connected by a line.

2. Method

2.1. Description

The `vbroad` determination is part of the STA and MTA chains of the spectroscopic pipeline that is meant to be only applied on single-line spectra without emission. Suspected line emission or binarity (Sartoretti et al. 2022; Katz et al. 2023; Damerdji et al., in prep.) is usually detected by the pipeline. About 28 000 targets were flagged for emission in their spectra, and ~40 000 (Katz et al. 2023) were flagged as SB2 candidates by the pipeline. Therefore, these were not processed for (single-line) RV and `vbroad`. For all the other cases, the measurement is performed on a transit- by-transit basis by maximising the top of the combination of the cross-correlation functions (CCF) that result from the correlation of all the valid CCD strip spectra by the template, which is broadened to a given `vbroad` value (upper panel in Fig. 1). The template is the continuum-normalised and LSF-broadened synthetic spectrum whose set of APs in the library is most similar to the target parameters. The library of synthetic spectra we adopted is described in Blomme et al. (2017) and does not include any additional line-broadening (e.g. ignores macroturbulence). For stars cooler than 7000 K, most of the parameter values were taken from intermediate results of Apsis (Creevey et al. 2023) with an earlier version of GSP-Phot[3] and of GSP-Spec[4] (Andrae et al. 2023; Recio-Blanco et al. 2023; these papers describe the results obtained with *Gaia* DR3 BP/RP and RVS spectra), as well as with DR2 spectra, while for the hotter stars, they were derived as explained by Blomme et al. (2023) to reduce the impact of known mismatches on the RV determination (see Sartoretti et al. 2022, for more information about the STA pipeline and the determination of `vbroad`.). Furthermore, during the pipeline testing and validation process that preceded the operational run, no time was left to assess the impact of deblended spectra on the measurement of `vbroad`. It was therefore decided that we remain conservative and derive it using only non-blended spectra.

[1] Extended Stellar Parametrizer – Hot Stars.
[2] Astrophysical ParameterS Inference System.
[3] General Stellar Parametrizer from Photometry.
[4] General Stellar Parametrizer from Spectroscopy.

The CCF maximisation procedure allows vbroad to vary in three iterations from 0 to 600 km s^{-1} (i.e. each iteration reduces the step around the maximum), with a minimum vbroad step of 5 km s^{-1}. For each transit, the final result is obtained by adopting the procedure described in David & Verschueren (1995) to mitigate the impact of discretisation. As shown in Fig. 1 (upper panel), the approach combines the solution obtained by fitting two parabolas through three and four points (see their Eq. (19)) taken at about the top of the function defined by the CCF maxima estimated at different vbroad values. Hence, we assumed that the top of the function to fit is nearly symmetrical. In practice, the existing asymmetry makes the procedure less effective, but it is still meaningful in most cases.

We show in the lower panel of the same figure how the sensitivity of the CCF maximisation varies with the effective temperature and the spectroscopic content of the RVS. The dependence of the CCF maxima on vbroad is stronger at lower values and flattens with increasing $T_{\rm eff}$, especially above 7500 K. While one estimate per transit is determined (at the STA stage), the target vbroad that is published in the *Gaia* DR3 catalogue is the median taken (during the MTA stage) over at least six valid transits (Sect. 2.2), and the corresponding uncertainty is assumed to be equal to the standard deviation.

2.2. Post-processing filtering

We report the vbroad estimates published in the *Gaia* DR3 catalogue. Prior to post-processing, 7 218 658 vbroad estimates were available for sources with $G_{\rm RVS} \leq 12$. About 50% of the initially available results were filtered out after quality assessment. We established the filtering criteria during the validation of the pipeline results as follows:

1. Most vbroad values and uncertainties of targets with fewer than six transits showed dubious features and were therefore removed from the catalogue (i.e. we kept the value when $N_{\rm t} \geq 6$).
2. Because the rotational convolution is performed in Fourier space with a sampling of the spectra that was optimised for RV determination (~4 km s^{-1}), all values lower than 4 km s^{-1} are questionable. For this reason, we filtered out all estimates lower than or equal to 5 km s^{-1} (i.e. we kept them when vbroad $>$ 5 km s^{-1}).
3. vbroad values higher than 500 km s^{-1} were removed as they formed a noticeable and likely non-physical overdensity in the observed velocity distribution (i.e. we kept them when vbroad $<$ 500 km s^{-1}).
4. In the very cool temperature range and in the valid vbroad domain, we found too few catalogue values to validate the measurements. It was therefore decided to filter out the estimates obtained for stars cooler than 3500 K (i.e. we kept them when $T_{\rm eff} \geq 3500$ K).
5. For consistency reasons, vbroad measurements obtained on data without a valid radial velocity were deleted (i.e. we kept them when the RV was valid). With the previous filter taken into account, only measurements obtained for targets with $T_{\rm eff}$ ranging from 3500 K to 14 500 K are therefore published.

2.3. Expected accuracy and significance

The Radial Velocity Spectrometer covers the 846–870 nm wavelength domain (Cropper et al. 2018). Its median resolving power is 11 500. The selection of the wavelength domain is a compromise between technical and astrophysical constraints. The goal is to measure the most accurate radial velocities for the majority of the stellar populations seen by *Gaia* with the most accurate astrometry. The calcium triplet observed in this domain was found to be the best choice (e.g. Munari 1999) because it remains strong at various metallicity regimes in the spectra of F-, G-, and K-type stars.

While rotational broadening may affect the RV determination, the RVS domain is not well suited to determine it accurately. This is especially the case for stars hotter than 7000 K, in which the main features are due to intrinsically broad lines (higher members of the Paschen series and Ca II triplet lines), which by nature are strongly blended with one another (e.g. Fig. 17 in Cropper et al. 2018). Furthermore, with the adopted method, the measurement of $V \sin i$, or vbroad strongly depends on the quality of the template spectrum, which in turn assumes a good knowledge of the astrophysical parameters and of the phenomena that shape the line profiles. Consequently, an incorrect template will automatically lead to an incorrect estimate.

To test the impact of the $T_{\rm eff}$ template mismatch by ignoring noise and assuming a perfect knowledge of the LSF (i.e. for the exercise, we assumed a Gaussian LSF and a resolving power of 11 500), we ran a partial version of the pipeline that derives vbroad on synthetic spectra and chose templates with various $T_{\rm eff}$ mismatches or errors for the same target spectrum. Figure 2 shows the results obtained at different $V \sin i$ and effective temperature values on the main sequence (MS). We extended the explored range of $T_{\rm eff}$ mismatches up to ±2000 K to cover most of the possible cases, but fewer errors or mismatches are expected especially for the late-type stars. The impact of the template mismatch depends on the sign and absolute value of the $T_{\rm eff}$ error. In most cases, the vbroad estimate is more sensitive to positive temperature errors (i.e. the template $T_{\rm eff}$ is lower than the target $T_{\rm eff}$) when the template usually exhibits more spectral features. In these cases, the pipeline tends to overestimate vbroad. On the other hand, in A-type stars, where the blends between the Paschen and calcium triplet lines dominate, the accuracy of vbroad is the most sensitive to the $T_{\rm eff}$ error. A similar negative impact of the $T_{\rm eff}$ error on the RV estimates of the A-type stars has also been noted (Katz et al. 2019), and led to the redetermination of the APs (Blomme et al. 2023), as well as to a first estimate of the line-broadening by the pipeline before RV and vbroad were derived. For this reason, as the same template is used for RV and vbroad determination, the effect of the template mismatch due to inaccurate APs is expected to be mitigated for the A- and B-type stars.

Furthermore, we conducted a series of Monte Carlo (MC) simulations to better illustrate the limitations of the technique or pipeline and of the wavelength domain we adopted, as well as of the instrument (in particular its resolving power). One MC sample was made up of 1000 cases at a fixed $T_{\rm eff}$, $\log g$, [M/H], and $G_{\rm RVS}$ magnitude. Each of these MC realisations assumed a different number of transits ($N_{\rm t}$) and $V \sin i$, and each CCD strip spectrum had its own photon noise. The number of transits was chosen randomly, but followed the observed $N_{\rm t}$ distribution (Fig. 3), and $V \sin i$ ranged from 0 to 600 km s^{-1} and followed a uniform random distribution. No template mismatch was introduced during the tests, and the same post-processing filters were applied (e.g. only cases with more than five transits were considered, see Sect. 2.2).

The main outcomes of the tests are illustrated in Fig. 4, where vbroad is plotted as a function of $V \sin i$, and in Fig. 5 ,which shows how the relative error varies with $V \sin i$. Both figures were made for different combinations of the effective temperature and magnitude. At a $V \sin i$ lower than 20 km s^{-1},

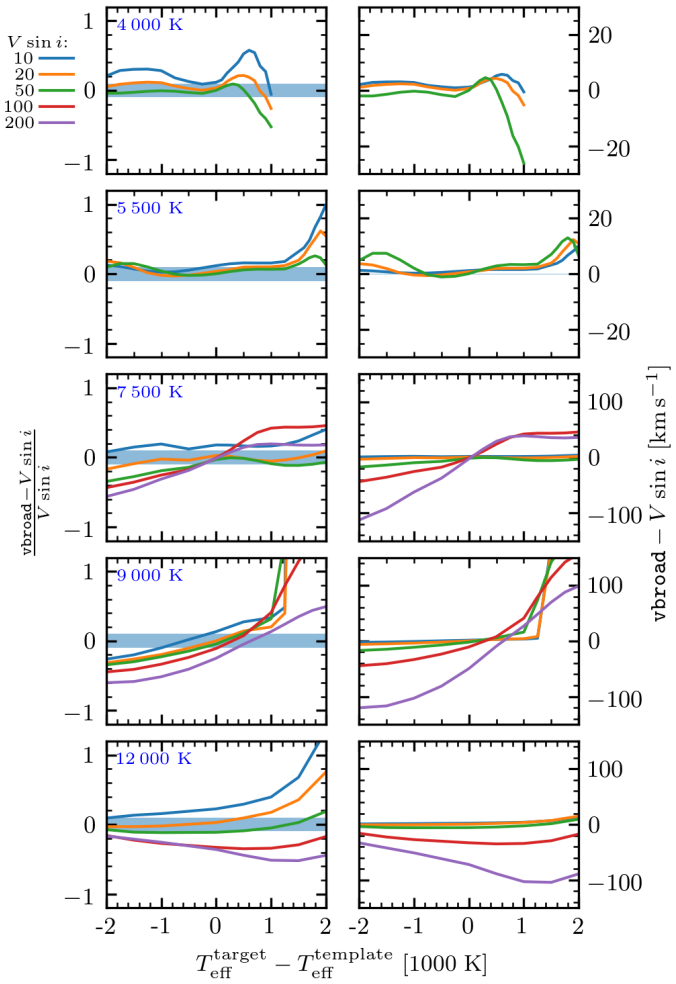

Fig. 2. Relative (*left panels*) and absolute (*right panels*) vbroad – $V \sin i$ residuals plotted as a function of the $T_{\rm eff}$ error made during the selection of the template spectrum. $V \sin i$ stands for the projected rotational velocity adopted to construct the simulation, and vbroad is the estimate provided by the pipeline. Different $V \sin i$ (see the legend and colour -coding) and 'true' $T_{\rm eff}$ estimates are considered. In the left panels, the blue hatches identify the domain in which the errors are within 10% of the expected value.

vbroad tends to be systematically larger than $V \sin i$ due to the resolving power, the wavelength sampling, and the approach we adopted. At higher values, the error remains within 10% for the brightest magnitudes with a vbroad measurement that tends to be underestimated. When the magnitude becomes fainter, the results degrade rapidly at $T_{\rm eff} > 7500$ K. In the temperature regime of the early A- and B-type stars, the impact of the broadening on the Paschen lines remains the main available source of information. We show in Fig. 6 how the CCF maximum varies with vbroad, $V \sin i$, $G_{\rm RVS}$, and $T_{\rm eff}$ above 7500 K for one transit and one noise realisation. At 9000 K, where the Paschen lines are largest or broadest and are blended with the calcium triplet, the offset strongly increases with $V \sin i$ (Fig. 6, upper left panel). The CCF centre is most sensitive (i.e. its gradient with vbroad varies more rapidly) at lower $V \sin i$ for $G_{\rm RVS} = 8$, but it rapidly becomes noisier with increasing magnitude (Fig. 6, lower left panel). Conversely, at 12 000 K, and with a spectrum dominated by the overlapping Paschen lines, the method tends to be less sensitive to low $V \sin i$ (i.e. smaller curvature; see right upper panel of Fig. 6) and still decreases rapidly with magnitude

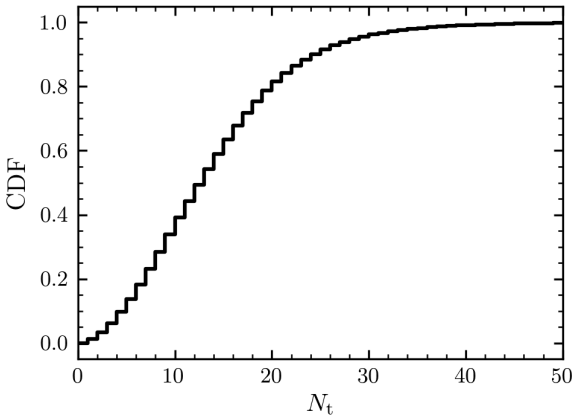

Fig. 3. Cumulative distribution function of the number of unblended transits ($N_{\rm t}$) before post-processing.

(Fig. 6, right lower panel). Together with the limitations inherent to our measuring technique, these effects are at the origin of the features seen at low $V \sin i$ in the lower right panel of Figs. 5 and 4 ($T_{\rm eff} = 12\,000$ K, $G_{\rm RVS} = 11$).

3. Results

The post-processed results of the vbroad determination algorithm are to be found in the gaia_source table. Fields vbroad and vbroad_error contain the vbroad estimate and its standard deviation, respectively. The number of transits considered to compute the median is given in vbroad_nb_transits.

The impact of the successive post-processing filters (Sect. 2.2) is summarised in Table 1. Of the 7 218 658 vbroad measurements initially available for targets brighter than $G_{\rm RVS} = 12$, the *Gaia* DR3 catalogue contains 3 524 677. Their magnitude and $T_{\rm eff}$ distributions are given in Fig. 7. Of these, the spectra of 428 529[5] stars are published with an expected resolution lower than the CCD spectra (Seabroke et al., in prep.), however. As a consequence of the post-processing (Sect. 2.2), the adopted template $T_{\rm eff}$ ranges from 3500 K to 14 500 K. No measurement is expected for stars fainter than magnitude 12. However, during the processing, the decision is based on a $G_{\rm RVS}$ estimate that is slightly different from the one published in the field grvs_mag (Sartoretti et al. 2023) which is plotted in Fig. 7 and explains that a fraction of fainter targets is present. The variation in vbroad_error with vbroad is represented in Fig. 8. The stellar population of *Gaia* is dominated by slowly rotating FGK stars, which produces the overdensity at vbroad < 20 km s^{-1}.

Figure 9 displays the variation of the relative uncertainty $\frac{\texttt{vbroad\_error}}{\texttt{vbroad}}$ as a function of $G_{\rm RVS}$ magnitude for cool ($T_{\rm eff} < 7500$ K) and hot stars ($T_{\rm eff} \geq 7500$ K). The relative uncertainty remains better than 20% for targets brighter than $G_{\rm RVS} = 9$, but it increases significantly for fainter objects: it reaches 60% at $G_{\rm RVS} = 11$ until it exceeds 100% at the faint limit.

4. Comparison with other catalogues and surveys

The large spectroscopic surveys that have been initiated in the past two decades have published a huge quantity of rotational broadening measurements. These homogeneous sets of values

[5] The number of available spectra was obtained by forming the following query: SELECT * FROM user_dr3int6.gaia_source WHERE vbroad is not null and has_rvs ='t'.

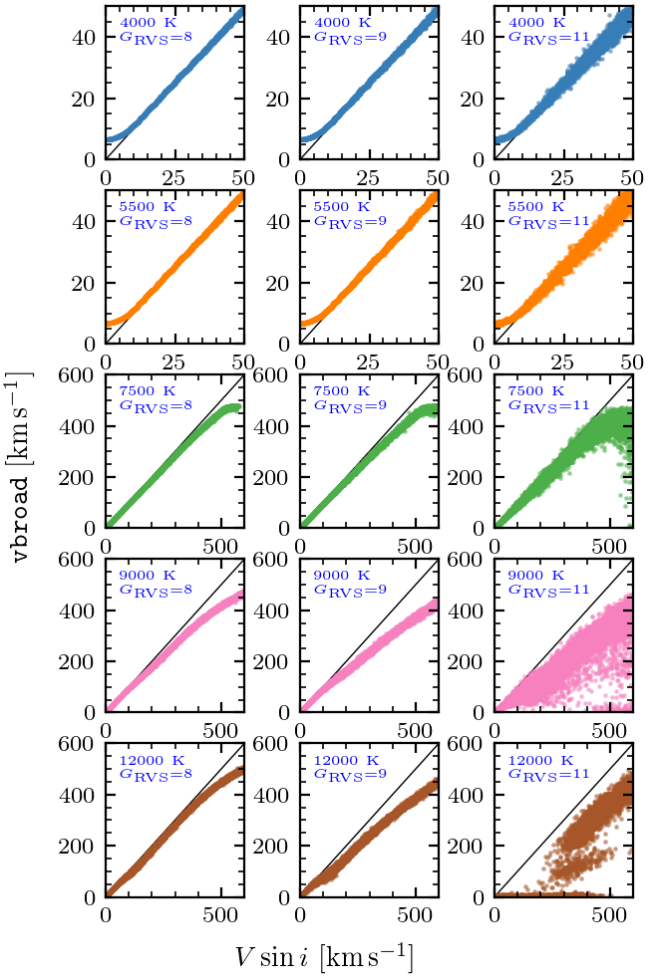

Fig. 4. Monte Carlo simulations: `vbroad` as a function of $V \sin i$ for various G_{RVS} magnitudes and effective temperatures. The identity relation is represented by the black line. The colour -coding is the same as in Fig. 5.

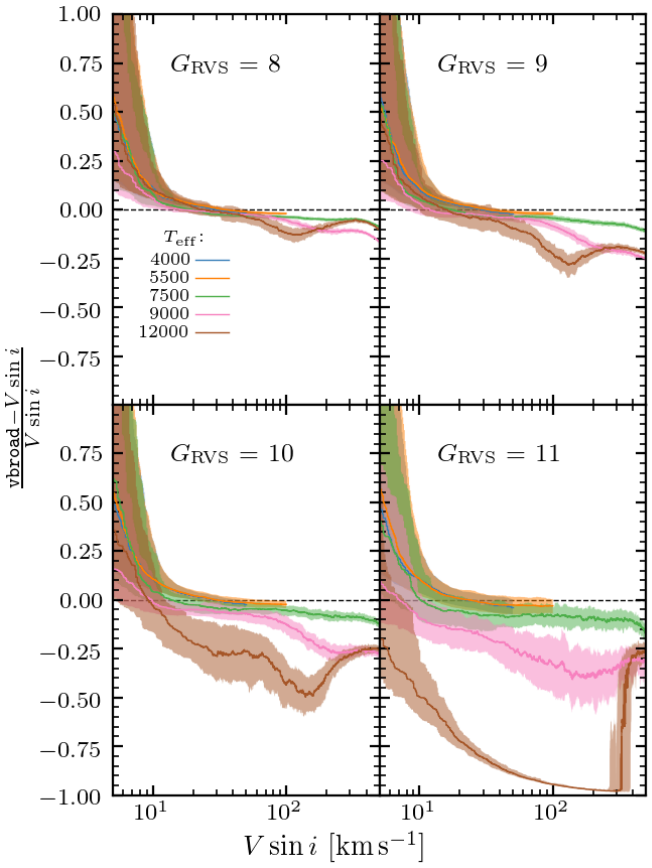

Fig. 5. Monte Carlo simulations: Relative (`vbroad` − $V \sin i$) residuals as a function of $V \sin i$ for various G_{RVS} magnitudes and effective temperatures (coloured lines). The 15–85% interquantile range is represented by shades.

provide a way to compare the different scales of rotational broadening measurements, each of which is affected by their own biases and uncertainties that originate from determination methods or from instrumental configuration. Four different catalogues were chosen for the comparison with the *Gaia* DR3 `vbroad` parameters: RAVE DR6 (Steinmetz et al. 2020), GALAH DR3 (Buder et al. 2021), APOGEE DR16 (Jönsson et al. 2020), and LAMOST DR6 (OBA stars) (Xiang et al. 2022). In addition to these, the compilation made by Głębocki & Gnaciński (2005, hereafter referred to as GG) allows a comparison for `vbroad` values that were determined on brighter targets. An overview of the catalogues and surveys we considered is given in Fig. 10. It shows the coverage in terms of T_{eff}, G_{RVS}, and $V \sin i$ for the different comparison samples. The spectral characteristics of the catalogues and the size of the comparison samples are summarised in Table 2.

The RAVE pipeline operations are described in RAVE DR2 (Zwitter et al. 2008) and in the DR3 (Siebert et al. 2011) papers. To derive the stellar parameters, they used a penalised χ^2 technique to model the observed spectrum as a weighted sum of template spectra with known parameters. Due to the low spectral resolution (Table 2) and the resulting difficulty of measuring low rotational velocities, they chose to restrict the dimension of their grid of templates in $V \sin i$. Their library of synthetic spectra is hence poorly populated at the low end of rotational broadening: their low $V \sin i$ values are only 10, 30, and 50 km s^{-1}. The macroturbulence velocity is not part of the atmospheric parameters that are taken into account in the RAVE pipeline.

For LAMOST, Xiang et al. (2022) analysed the low-resolution survey spectra of hot stars, specifically OBA, and they adapted The Payne neural network spectral modelling method to hot stars to determine the stellar labels of the sample targets. At the resolution of LAMOST, they were unable to distinguish macroturbulence from rotational velocities, and their $V \sin i$ estimates include its contribution.

In the APOGEE pipeline (García Pérez et al. 2016), the spectral analysis is performed with FERRE (Allende Prieto et al. 2006), which finds the best-fitting stellar parameters describing an observed spectrum by interpolating in a grid of synthetic templates. This grid, however, is restricted in the $V \sin i$ dimension to the values 1.5, 3, 6, 12, 24, 48, and 96 km s^{-1}. $V \sin i$ is only determined for dwarf stars, while in the giant sub-grids, a macroturbulence velocity broadening, calibrated as a function of metallicity (Jönsson et al. 2020), is adopted instead.

In GALAH, the stellar atmospheric parameters are derived using the spectrum synthesis code Spectroscopy Made Easy (Piskunov & Valenti 2017). In the corresponding catalogue, the $V \sin i$ parameter is cautiously called v_{broad} as it is fitted by setting the macroturbulence to 0 because macroturbulent and rotational broadening influences are degenerate at the resolution of GALAH (Buder et al. 2021).

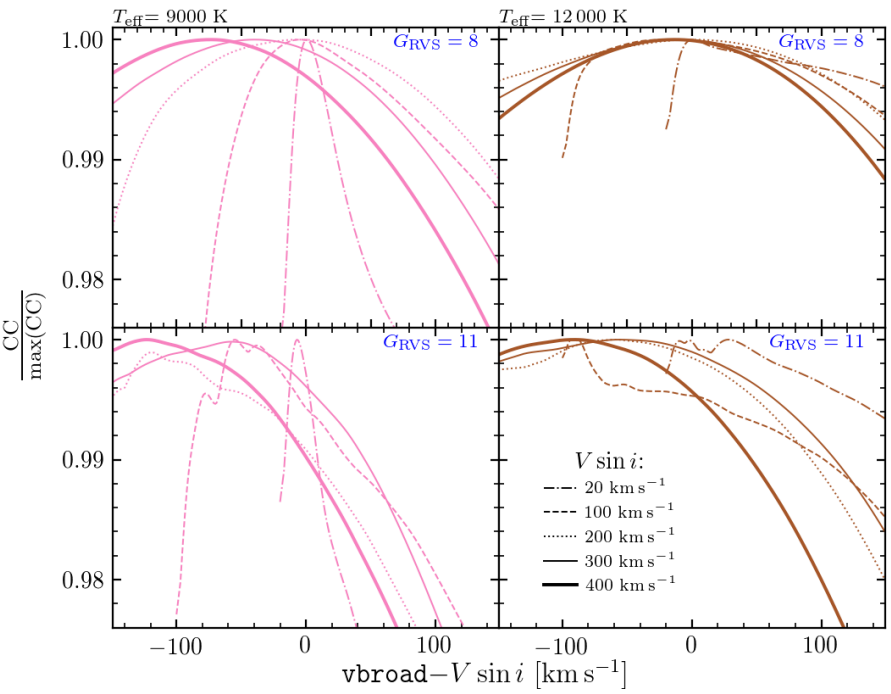

Fig. 6. Example of the variation in CCF maximum with $T_{\rm eff}$, $G_{\rm RVS}$ (noted in blue in the upper right corner of each panel), `vbroad`, and $V \sin i$ (see line styles in the legend). Each curve represents only one noise realisation (i.e. one transit) and is normalised to its highest value at a given $V \sin i$. See also Fig. 1.

Table 1. Impact of the post-processing on the number of remaining `vbroad` estimates.

#	Filter	$N_{\rm rem.}$
	$G_{\rm RVS} \leq 12$	7 218 658
1	$N_{\rm t} \geq 6$	5 327 091
2	`vbroad` > 5 km s^{-1}	3 717 427
3	`vbroad` < 500 km s^{-1}	3 717 143
4	$T_{\rm eff} \geq 3500$ K	3 675 448
5	RV is valid	3 524 677

Notes. $N_{\rm rem.}$ is the number of remaining targets after applying the filters sequentially. The filters are listed with their item number (#) from Sect. 2.2.

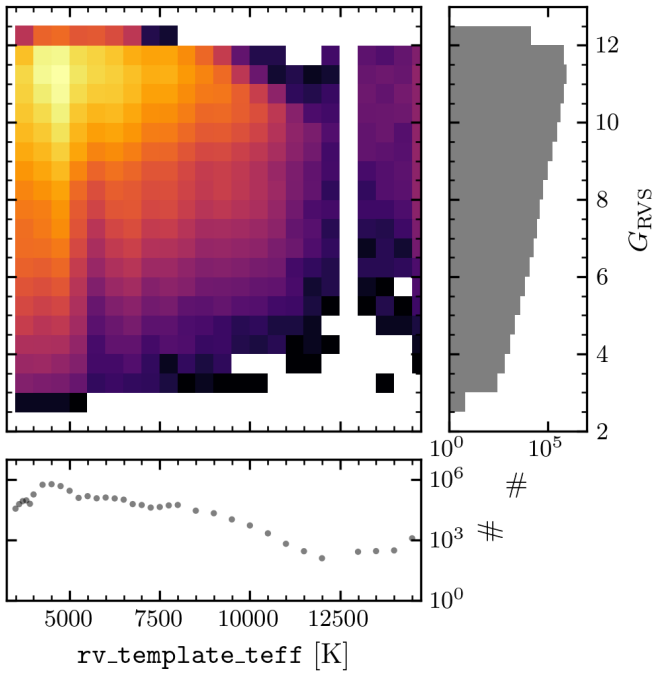

Fig. 7. Distribution of the *Gaia* DR3 `vbroad` catalogue with magnitude and effective temperature. *Lower panel*: effective temperature of the adopted template (`rv_template_teff`) distribution. Our template library does not contain spectra with $T_{\rm eff}$ = 12 500 K, which translates into a gap in the distribution at the same temperature. *Right panel*: $G_{\rm RVS}$ magnitude (`grvs_mag`) distribution.

We used the mean $V \sin i$ determinations given by Głębocki & Gnaciński (2005). The main contributions come from Nordström et al. (2004), providing about 12 500 $V \sin i$ determined by cross-correlation technique for F- and G-dwarf stars, notably complemented by almost 3000 $V \sin i$ derived from FWHM for B- and A-type stars (Abt et al. 2002; Abt & Morrell 1995). The catalogue built by Głębocki & Gnaciński (2005) partly inherits the discretisation of $V \sin i$ from the publications it compiles. This discretisation can produce an overestimation of the residuals for low $V \sin i$ values.

4.1. Selection of the comparison samples

The catalogues we used to compare the line-broadening scales provide in some cases a quality assessment of their data. We used these assessments to only keep the most reliable estimates as follows:

- In the GALAH survey, the flag `flag_sp` reflects the quality of the spectroscopic parameters, and only common targets with `flag_sp`= 0 were taken into account.
- The APOGEE catalogue also provides a flag, `f_Vsini`, that assesses the quality of the published $V \sin i$ determinations. Only common targets with `f_Vsini` = 0 are considered here.
- RAVE data were selected on the basis of the height of the CCF given in the catalogue: `hcp` > 0.9.
- LAMOST data were selected on the basis of their reduced χ^2 such that `CHISQ_RED` < 5.
- The quality of the compiled data from GG was assessed upon the flag `n_vsini` that indicates when the precision

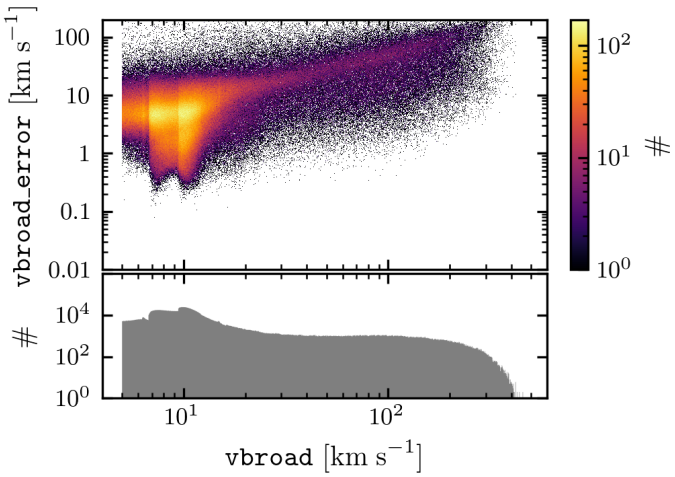

Fig. 8. Distribution of `vbroad` and `vbroad_error`. *Upper panel*: `vbroad_error` vs. `vbroad`. *Lower panel*: corresponding distribution of the number of targets in each `vbroad` bin.

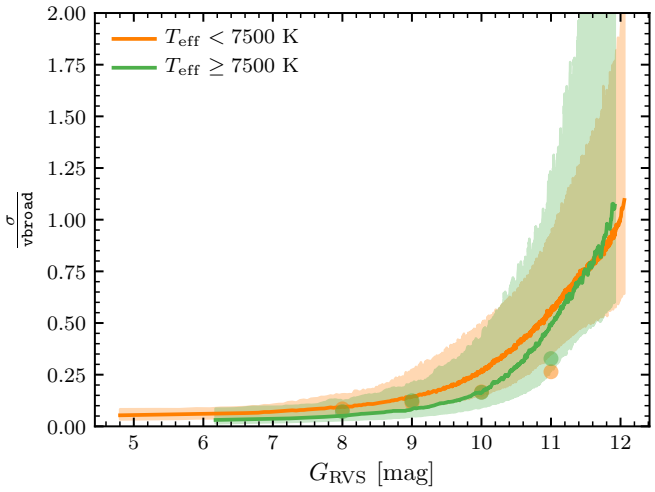

Fig. 9. Relative uncertainty on `vbroad` as a function of $G_{\rm RVS}$ magnitude for two $T_{\rm eff}$ ranges. Thick lines are the running median values (over 2000 targets), and the coloured regions correspond to the associated 15% and 85% quantiles. The filled circles are the relative uncertainties corrected for the z-score estimates performed in Sect. 5.

is poor (':') or when the datum solely originates from Uesugi & Fukuda's compilation (1982), whose quality was already questioned by Soderblom et al. in 1989. Only targets with an empty `n_vsini` flag were used.

Figure 10 shows the data that were discarded from the comparison samples using the criteria listed above as grey bars. The cuts produced by this selection in the $V \sin i$ distributions are clear: all targets with $V \sin i \gtrsim 70\,\mathrm{km\,s^{-1}}$ and $V \sin i \gtrsim 100\,\mathrm{km\,s^{-1}}$ are removed from the APOGEE and GALAH comparison samples, respectively.

4.2. Two-by-two comparisons

Figure 11 displays the two-by-two comparisons we made with the catalogues. The five panels on the left compare the *Gaia* DR3 `vbroad` to the ground-based measurements, while the remaining panels show internal cross-matches between the catalogues, without restricting the comparison to the intersection with the *Gaia* DR3 values. As the GG compilation mainly contains bright

Table 2. Characteristics of the comparison catalogues.

Catalogue	Size	Resolution	Spectral range [nm]
GG	10 821	various	various
RAVE	212 622	7500	841.0–879.5
APOGEE	21 078	22 500	1514.0–1694.0
GALAH	84 464	28 000	471.3–490.3
			564.8–587.3
			647.8–673.7
			758.5–788.7
LAMOST	25 770	1800	380.0–900.0

Notes. The size is that of the comparison sample.

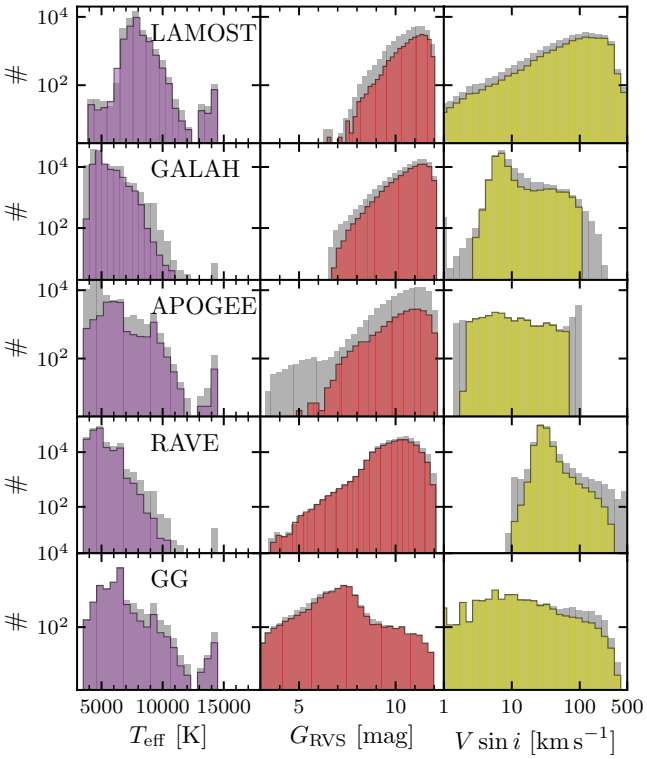

Fig. 10. Overview of the intersection of stars with published *Gaia* DR3 `vbroad` with the reference catalogues or surveys: GG (Głębocki & Gnaciński 2005), RAVE (Steinmetz et al. 2020), GALAH (Buder et al. 2021), APOGEE (Jönsson et al. 2020), and LAMOST (Xiang et al. 2022). *Left panel*: $T_{\rm eff}$ distribution (i.e. `rv_template_teff`). *Central panel*: $G_{\rm RVS}$ distribution. *Right panel*: $V \sin i$ distribution. The additional grey bins represent the part of catalogue intersections that were discarded in the cleaning process (see Sect. 4.1).

targets, its intersection with the other ground-based surveys is limited. The LAMOST survey observes the northern hemisphere, whereas RAVE and GALAH are focussed on the southern hemisphere. In addition to being dedicated to hot stars, its intersection with the other ground surveys is therefore also limited. The APOGEE footprint covers both hemispheres.

We emphasise that a fraction of these comparisons can be contaminated by incorrect cross-identifications when the different catalogues were cross-matched (Pineau et al. 2020) by positions in the sky. Rotational broadening determinations can also be biased by undetected spectroscopic companions or by stellar

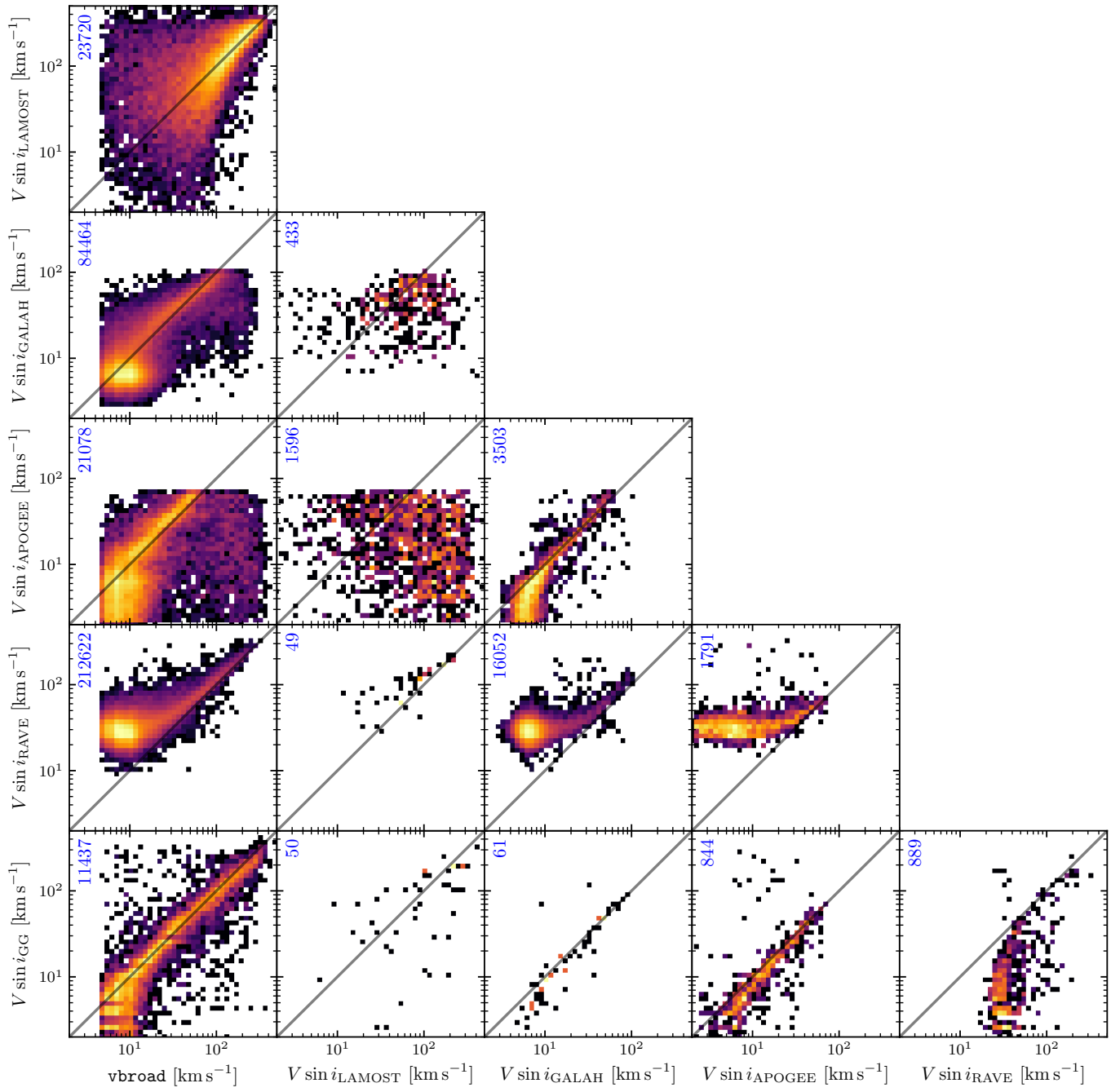

Fig. 11. Comparison with other catalogues: One-to-one comparisons of line-broadening measurements of the considered sources, including *Gaia* DR3. The velocity scales are logarithmic, as is the density colour scale. Sizes of comparison samples are indicated in the upper left corners, and the one-to-one relation is represented by the diagonal black line.

activity, and these biases can affect the comparison catalogues differently depending on spectral coverage, resolving power, and so on.

The logarithmic scales in Fig. 11 allow us to overview the shifts at low and high line-broadening values. Overdensities are present in the low-velocity lower left panel corner for the comparison samples (GALAH, APOGEE, and RAVE) that are dominated by cool slowly rotating stars. Comparisons with GALAH and APOGEE data, performed with a higher resolving power, show that the `vbroad` determinations in *Gaia* DR3 are overestimated at lower $V \sin i$ partly due to the lower resolution in the RVS spectra. The spectral resolution in the RAVE survey is lower than in the RVS, and their rotational velocity determinations, in addition to being rounded to integer values, reach a plateau at about 20 km s^{-1} (only 2% of the $V \sin i$ in the RAVE comparison sample are lower than 20 km s^{-1}).

The right upper part of the panels is only populated with the catalogues that contain fast-rotating stars and are able to determine high rotational velocities. The APOGEE survey has a hard upper limit at 96 km s^{-1}, which partly explains why the lower right quadrant of the *Gaia* DR3-APOGEE panel is significantly populated. The comparison with LAMOST data is very dispersed because of the much lower resolution and possibly the larger effect of template mismatch. The catalogue content mainly

consists of OBA targets ($T_{\rm eff}$ > 7500 K), however, therefore it allows an assessment of the vbroad quality in the higher velocity range ($V \sin i \gtrsim 100\,{\rm km\,s^{-1}}$). Whereas the comparison with GG seems in good agreement as soon as vbroad $\gtrsim 15\,{\rm km\,s^{-1}}$, a trend appears at high values (vbroad $\gtrsim 200\,{\rm km\,s^{-1}}$), where vbroad determinations are systematically higher than their GG counterparts.

The correlation and correspondences with the catalogues we considered tend to confirm that the *Gaia* DR3 vbroad is a sensible measurement of the RVS line-broadening. However, it also shares the limitations at lower $V \sin i$ of other catalogues.

4.3. Residuals as a function of $T_{\rm eff}$

In order to quantify the residuals as a function of the observed magnitude and effective temperature, the comparison samples were subsampled based on $G_{\rm RVS}$ (grvs_mag) and $T_{\rm eff}$ (rv_template_teff). It therefore gives a more detailed view of the trends visible in the first column of Fig. 11. The magnitude ranges are centred on $G_{\rm RVS}$ = 8, 9, 10, and 11 (except for those for GG, which are shifted 2 mag brighter), and have a width of 1 mag, while the effective temperature domains are taken at $T_{\rm eff} = 4000 \pm 250$ K, 5500 ± 250 K, 7500 ± 500 K, 9000 ± 500 K, and $12\,000 \pm 1000$ K.

Figure 12 shows the resulting distribution of the residuals with magnitude and effective temperature. We only plot subsamples with more than 80 targets, while the width of the running window represents one-twelfth of the total number of measurements in the subsample. Only a few comparison ensembles are able to provide information about the residuals for the coolest ($T_{\rm eff}$ at 4000 K) or hottest targets ($T_{\rm eff}$ range at 12 000 K).

When $T_{\rm eff}$ subsamples are present at different magnitudes for the same catalogue, there is no significant impact on the residual offsets on average, while their dispersion tends to increase with $G_{\rm RVS}$. As a global tendency, the residuals show that the *Gaia* DR3 vbroad determinations are overestimated at low $V \sin i$ compared to other catalogues. By comparison with GG, GALAH, and APOGEE, this overestimation appears below $\sim 12\,{\rm km\,s^{-1}}$. At higher values and when we exclude GG, vbroad appears to underestimate $V \sin i$ by magnitudes that depend on $T_{\rm eff}$ and $G_{\rm RVS}$.

Comparison with GG shows a good agreement for bright targets (6–8 mag), without any notable bias for velocities higher than $\sim 15\,{\rm km\,s^{-1}}$. At magnitude $G_{\rm RVS}$ = 9, GG is no longer dominated by its largest contributors and starts being a compilation of only small heterogeneous data sets: the 127 targets that populate the right panel for GG in Fig. 12 may not be representative of the residual distribution. Moreover, the same $T_{\rm eff}$ subsample at magnitude $G_{\rm RVS} \sim 9$ agrees better in comparisons with homogeneous catalogues such as GALAH or APOGEE.

For the comparison with RAVE data, Fig. 11 already showed that their low $V \sin i$ are systematically overestimated, regardless of the catalogue they are compared with. For velocities higher than $\sim 60\,{\rm km\,s^{-1}}$, however, the residuals with *Gaia* DR3 vbroad improve. They are around −10%, with a very small dispersion. This low scatter may originate in the spectral range, which is the same, and in the similar resolving power as for RVS spectra.

The much lower resolving power in LAMOST spectra dominates the observed residuals below $V \sin i \lesssim 100\,{\rm km\,s^{-1}}$. Above this value, the rotational broadening determinations are consistent for the $T_{\rm eff}$ range 7500 K, but the residuals significantly increase with magnitude for hotter targets.

5. Discussion

Figure 13 displays the variation in vbroad distribution as a function of the spectral type, as already shown by Royer (2014), and compares it with $V \sin i$ data from the GG comparison sample. The coloured density plot is based on 63 248 vbroad values of MS stars ($3.5 \leq \log g \leq 4.5$) brighter than $G_{\rm RVS}$ = 9. The contour plot is derived from 9262 $V \sin i$ values compiled by GG, with the same selection criterion on $\log g$.

The modes of the distribution seem consistent between vbroad and $V \sin i$. The top panel in logarithmic scale reproduces the overestimation of vbroad at low $V \sin i$, already illustrated by Figs. 11 and 12, shown here by spectral types later than F5. In the bottom panel, the contour low levels for hot stars do not perfectly coincide with the vbroad distribution counts, suggesting that high-velocity distribution tails are more extended in the *Gaia* DR3 catalogue. As a result, the median values are also higher by 8 to 28% from F0- to A0-type stars. This broadening of the *Gaia* DR3 data is produced by the trend observed between the two velocity scales in Fig. 11.

The catalogue-to-catalogue correlation and residual plots of Sect. 4 reproduce the two main features identified during the MC simulations (Sect. 2.3). The *Gaia* DR3 vbroad overestimates the low $V \sin i$ values, while it tends to underestimate the higher values. From the simulations (Fig. 2), we noted a significant impact of the template mismatches for the hot stars due to an incorrect $T_{\rm eff}$ estimate. The comparisons made with the OBA LAMOST catalogue above $100\,{\rm km\,s^{-1}}$ still present relative residuals (lower panels of Fig. 12) that are fairly consistent in magnitude with those found in the simulations (Fig. 5) when the effects of template mismatches are neglected.

However, the simulations (e.g. Fig. 4) also show that the quality of the results obtained above 7500 K rapidly degrades with magnitude above $G_{\rm RVS}$ = 10. In order to further investigate this degradation of the vbroad quality with magnitude for hot stars, the median vbroad is plotted as a function of $G_{\rm RVS}$ for different $T_{\rm eff}$ (Fig. 14), exploring the transition from spectra dominated by the Ca II triplet to spectra dominated by the Paschen series. There is no noticeable trend for 7000 K stars (dark gold colour), whereas a slight decrease of vbroad appears for 7500–8000 K stars (greenish curves) at $G_{\rm RVS} \gtrsim 11$. For hotter stars (shades of pink), the effect is striking and increases with temperature. In addition to this severe underestimation of vbroad at faint magnitude, we note an apparent cut in $G_{\rm RVS}$ that also increases with temperature. This incompleteness was already seen in Fig. 7 and is the combined result of the degradation of vbroad at faint magnitude with the post-processing filtering that discarded values with vbroad $< 5\,{\rm km\,s^{-1}}$.

Because these findings are consistent with the trends reported in Sect. 2.3, we used the MC simulation results to define a validity domain of the line-broadening estimate and based it on the quantities provided in the catalogue (i.e. rv_template_teff, vbroad, and vbroad_error). We list in Table 3 the vbroad domain in which the measurement has a probability higher than 90% to be within 2σ (where σ is assumed to be equal to the standard deviation) of $V \sin i$. We provide these validity ranges as a function of $G_{\rm RVS}$ and $T_{\rm eff}$. They represent the domains in which the vbroad measurement and its provided uncertainty are expected to be consistent with $V \sin i$ when template mismatches can be ignored.

The vbroad published in *Gaia* DR3 is the median value of a sample of $N_{\rm t}$ measurements (where the median value of the number of transits is 12, as shown in Fig. 3) made on transit spectra. During the validation, we decided to adopt their standard

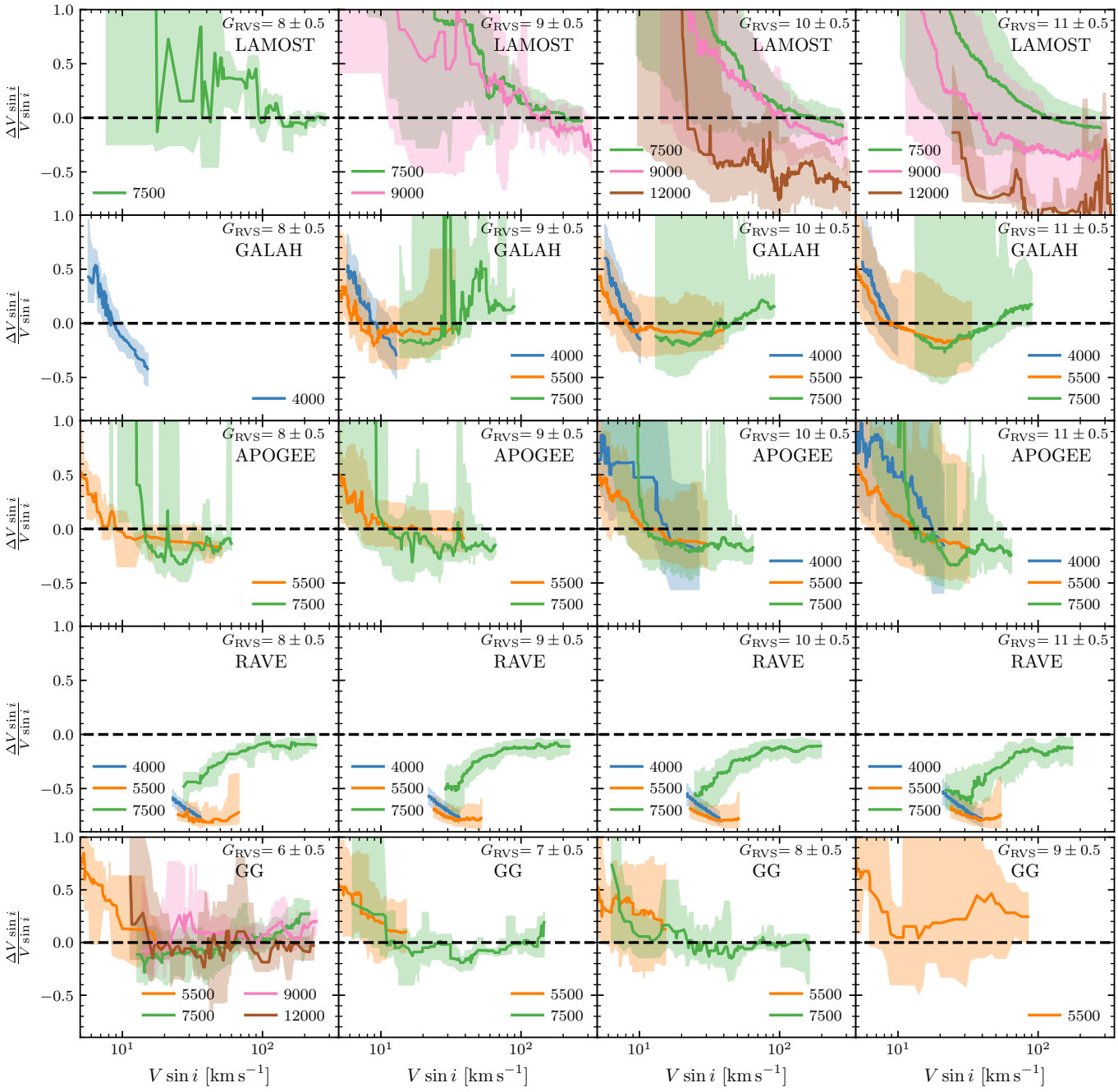

Fig. 12. Variation in relative residuals in `vbroad` as a function of the catalogue $V \sin i$ ($\Delta V \sin i$ = `vbroad` – $V \sin i$) for different ranges of effective temperature. The x-axis $V \sin i$ scales are from the comparison catalogues. *From left to right*: the panels inspect fainter ranges of magnitudes, 7.5–8.5, 8.5–9.5, and 9.5–10.5 mag, except for GG (last row), where the magnitude ranges are shifted 2 mag brighter. Thick lines represent the running median on the residuals, and the coloured regions correspond to the associated 15% and 85% quantiles. Each colour corresponds to the temperature given in the plots.

deviation as a measure of the uncertainty (Fig. 9). In Fig. 15 we compare this uncertainty to the scatter of the residuals of `vbroad` to the $V \sin i$ measurements published in those catalogues (GALAH and APOGEE) or $V \sin i$ ranges (LAMOST) that are expected to be less impacted by resolving power issues. We considered two $T_{\rm eff}$ domains representative of the spectroscopic content of the RVS, as well as various $V \sin i$ domains. On the basis of the dispersions measured in the residual distributions, we note that the uncertainty provided for the F-, G-, and K-type stars in the catalogue can be overestimated by a factor of ∼2 in the low `vbroad` regime and by a factor of ∼1.3 for larger `vbroad` estimates. On the other hand, the uncertainty tends to be less overestimated for the hotter stars (i.e. by a factor of ∼1.25).

The GALAH and LAMOST catalogues provide uncertainty estimates for the derived $V \sin i$, which offers the possibility of quantifying the change in z-score as a function of magnitude. As Fig. 15 shows residual distributions representative of the full common magnitude range with the catalogue, Table 4 lists the z-score results for the same $V \sin i$ ranges and different magnitude intervals. For cool stars, the dispersion decreases from ∼0.9

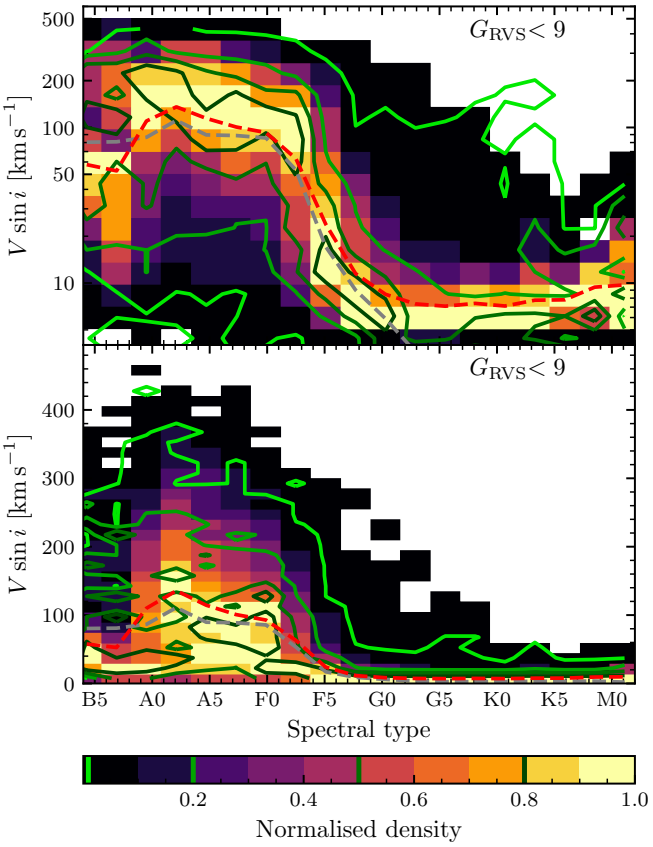

Fig. 13. Comparison of the distribution of `vbroad` as a function of spectral type (2D histogram, coloured by the linear number of targets), with the distribution of $V \sin i$ from GG (green contour lines). *Top panel*: the distribution with regular bins in logarithmic velocity scale, and the *bottom panel* displays the resulting distribution using a linear grid in velocity. The `vbroad` data are selected to be brighter than $G_{RVS} = 9$ and to be on the MS ($3.5 \leq \log g \leq 4.5$). $V \sin i$ data from GG are selected in the GG comparison sample (Table 2) with the same $\log g$ criterion. Spectral types are estimated on the basis of `rv_template_teff` by interpolating in the tables provided by Cox (2000). Dashed lines are the median values per bin of spectral types for the `vbroad` distribution (red) and the $V \sin i$ (grey). For each spectral type bin, the distribution is normalised to its maximum value. The colour bar superimposes the scale of the 2D histogram with the contour levels (0.01, 0.2, 0.5, and 0.8).

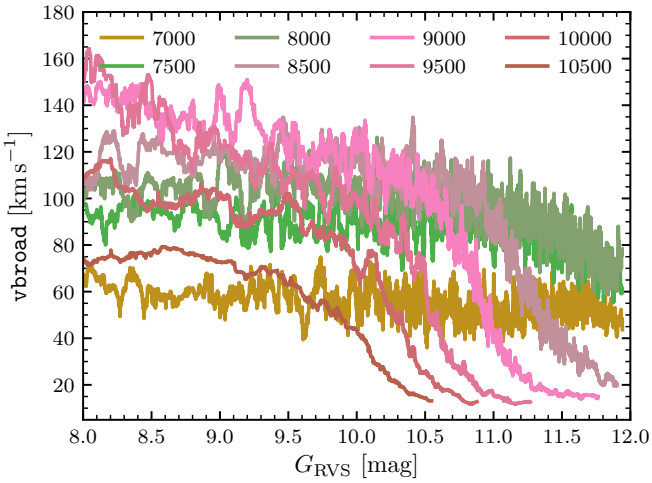

Fig. 14. Median value of `vbroad` as a function G_{RVS} for different T_{eff}. Temperatures are taken as exact `rv_template_teff` values, and median `vbroad` are derived on a running window of 200 points. Each colour corresponds to a T_{eff} labelled in the plot.

Table 3. `vbroad` validity domains derived from the MC simulations.

T_{eff} [K]	G_{RVS}	`vbroad` validity [km s^{-1}]	T_{eff} [K]	G_{RVS}	`vbroad` validity [km s^{-1}]
4000	8	>18	7500	8	12 – 110
	9	>14		9	10 – 140
	10	>12		10	9 – 280
	11	>10		11	8 – 330
5500	8	>18	9000	8	9 – 130
	9	>14		9	8 – 130
	10	>11		10	6 – 140
	11	>9		11	22 – 400
			12 000	8	10 – 250
				9	9 – 110
				10	9 – 40
				11	280 – 420

Notes. The validity domain was defined as the range of `vbroad` values in which the measurement has a probability higher than 90% to be within 2σ of $V \sin i$. Limit values above 30 km s^{-1} were rounded to the nearest ten.

to ~0.5 as the magnitudes become faint. This suggests that the uncertainty in the *Gaia* DR3 `vbroad` values is even more overestimated at fainter magnitudes. For the hotter fast-rotating stars, the comparison with LAMOST indicates that the `vbroad` uncertainty in the *Gaia* DR3 catalogue is probably underestimated for stars brighter than $G_{RVS} = 10$, but overestimated for fainter stars. We recall that the LAMOST comparison sample is dominated by stars with T_{eff} around 8000 K (Fig. 10), and the effect illustrated in Fig. 14 solely contributes to the tails of the z-score distribution. Figure 9 displays the average relative uncertainties at magnitudes $G_{RVS} = 8, 9, 10$ and 11, taking the MAD values from Table 4 as correction factors into account.

The final step of the validation shows the mapping of the median `vbroad` across the Hertzsprung-Russell diagram (HRD, see Fig. 16), using integrated photometry in the G, G_{BP}, and G_{RP} bands (Riello et al. 2021). For more than half the sample, extinction parameters are available from the Apsis pipeline (Creevey et al. 2023; Fouesneau et al. 2023; Andrae et al. 2023). The absorption in the G band, A_G, and the $G_{BP} - G_{RP}$ colour excess, $E(G_{BP} - G_{RP})$, are taken from ESP-HS (Creevey et al. 2023) for hot stars ($T_{eff} > 7500$ K, `ag_esphs`, `ebpminrp_esphs`) and from GSP-Phot for cooler ones (`ag_gspphot`, `ebpminrp_gspphot`). Both A_G and $E(G_{BP} - G_{RP})$ are taken into account to derive the positions $(G_{BP} - G_{RP})_0$ and M_G in the HRD. Only stars with parallaxes with a precision better than 10% are shown in Fig. 16. To limit the bias on `vbroad` observed for hot stars in Fig. 14, a filter in G_{RVS} depending on T_{eff} alone was preferred to using the validity domains listed in Table 3. These domains would have biased the statistical values in the HRD. The applied filtering limit varies linearly as a function of T_{eff},

$$G_{RVS} < 11.93 - 0.8087\,10^{-3}\,(T_{eff} - 7000), \text{ for } T_{eff} > 7000\,\text{K}. \quad (1)$$

The 0.1×0.1 mag bins in the HRD are plotted only if they contain at least ten stars. The diagram illustrates the large coverage of the parameter space by the *Gaia* DR3 `vbroad` catalogue: evolutionary stages from the MS to the giant branch and

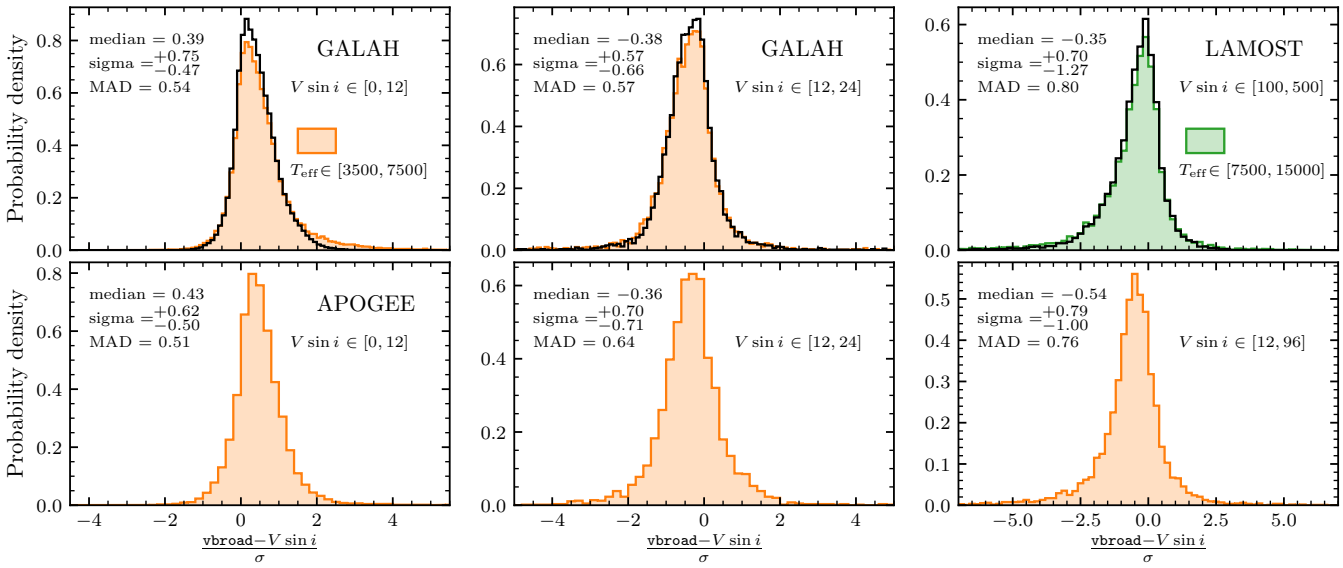

Fig. 15. Distribution of the residuals for different catalogues: GALAH and LAMOST (*top row*), and APOGEE (*bottom row*). Residuals are normalised by the uncertainty on `vbroad` in the *Gaia* DR3 catalogue. For the top panels, the superimposed black curve is the residual distribution normalised by the total uncertainty $\sqrt{\sigma^2_{\texttt{vbroad}} + \sigma^2_{V\sin i}}$. Each row corresponds to a selection in $T_{\rm eff}$ and $V \sin i$. Statistical estimators are given for each panel: Median value, upper and lower dispersions (85% quantile – median, and median – 15% quantile), and mean absolute deviation.

Table 4. z-score statistics from the comparison with the GALAH and LAMOST catalogues, normalised by the total uncertainty, for different ranges of magnitude and different ranges of $V \sin i$.

$G_{\rm RVS}$	$z_{\rm med}$	σ_{z+}	σ_{z-}	MAD	#
GALAH: $V \sin i \in [0, 12]$ km s^{-1}					
7.5 – 8.5	0.80	0.85	−0.84	0.86	784
8.5 – 9.5	0.69	0.84	−0.78	0.80	3884
9.5 – 10.5	0.50	0.75	−0.63	0.65	13306
10.5 – 11.5	0.33	0.52	−0.42	0.45	33760
GALAH: $V \sin i \in [12, 24]$ km s^{-1}					
7.5 – 8.5	−1.99	1.02	−1.38	0.96	48
8.5 – 9.5	−0.86	0.75	−1.20	0.82	238
9.5 – 10.5	−0.59	0.75	−0.61	0.60	1125
10.5 – 11.5	−0.35	0.53	−0.55	0.50	3006
LAMOST: $V \sin i \in [100, 500]$ km s^{-1}					
7.5 – 8.5	−0.34	1.98	−1.73	1.41	53
8.5 – 9.5	−0.18	1.55	−1.57	1.49	363
9.5 – 10.5	−0.34	0.93	−1.29	1.00	2198
10.5 – 11.5	−0.31	0.57	−0.98	0.67	5545

Notes. The median value of $(\texttt{vbroad} - V \sin i)/\sigma$, with $\sigma = \sqrt{\sigma^2_{\texttt{vbroad}} + \sigma^2_{V\sin i}}$, is given as $z_{\rm med}$; σ_{z+} and σ_{z-} are the upper and lower dispersions (85% quantile$-z_{\rm med}$, and 15% quantile$-z_{\rm med}$); MAD is the mean absolute deviation, and # the number of targets in the corresponding subsample.

the supergiants are present. The temperature scale in Fig. 16 is given as an indication, and it is based on the photometric temperatures, selected with the same criterion as for the extinction parameters (`teff_gspphot` for $T_{\rm eff} \leq 7500$ K, and `teff_esphs` for $T_{\rm eff} > 7500$ K). It roughly corresponds to the $T_{\rm eff}$ range 3500–14 500 K resulting from the applied filters (Sect. 2.2) on `rv_template_teff`.

The most prominent feature in the left panel is due to the rapid drop in the mean rotational velocity of stars around spectral type F5, known since Kraft (1967), and already seen in Fig. 13 for MS stars. More massive stars are generally rapid rotators, while less massive stars are characterised by a slow rotation. The evolutionary track of a solar metallicity 2 $M_\odot$ star, generated by a CMD 3.6[6] (Bressan et al. 2012; Chen et al. 2014, 2015; Tang et al. 2014; Marigo et al. 2017; Pastorelli et al. 2019, 2020), is overplotted to the upper MS from the zero-age main sequence (ZAMS) to the terminal-age main sequence (TAMS) as a reference.

The lower MS in the right panel ($M_{\rm G} > 5$) reveals the presence of the binary star sequence, 0.75 mag brighter than the MS of single stars. This sequence displays higher `vbroad` values in the left panel. In the range $1.1 < G_{\rm BP} - G_{\rm RP} < 1.4$ for example, the median `vbroad` values for the single sequence and the binary sequence are 9 and 14 km s^{-1}, respectively.

The lower MS of single stars seems to harbour a decrease in velocity from left to right. The overplotted isochrones, generated by CMD 3.6, correspond to two different ages (1 Gyr in black, 10 Gyr in grey) and three different metallicities: $[M/H] = -0.5, 0$, and $+0.5$, from left to right. They illustrate the fact that the thickness of the lower MS is dominated by a spread in the metallicity distribution and is not an evolutionary effect. This suggests that this trend in `vbroad` might be due to mismatches in metallicity between the spectra and the templates: a template broadened with a lower `vbroad` value has deeper lines and can fit an observed spectrum with a higher metallicity better. This therefore rules out the possibility of using the *Gaia* DR3 `vbroad` values as a gyrochronological tool and of inferring anything about stellar ages.

5.1. Effect of the macroturbulence

When measuring `vbroad`, no distinction is made between stellar rotation and other mechanisms that contribute to broadening the spectral lines at constant equivalent width. In particular, no effort is made to remove or derive the contribution of the

[6] http://stev.oapd.inaf.it/cmd

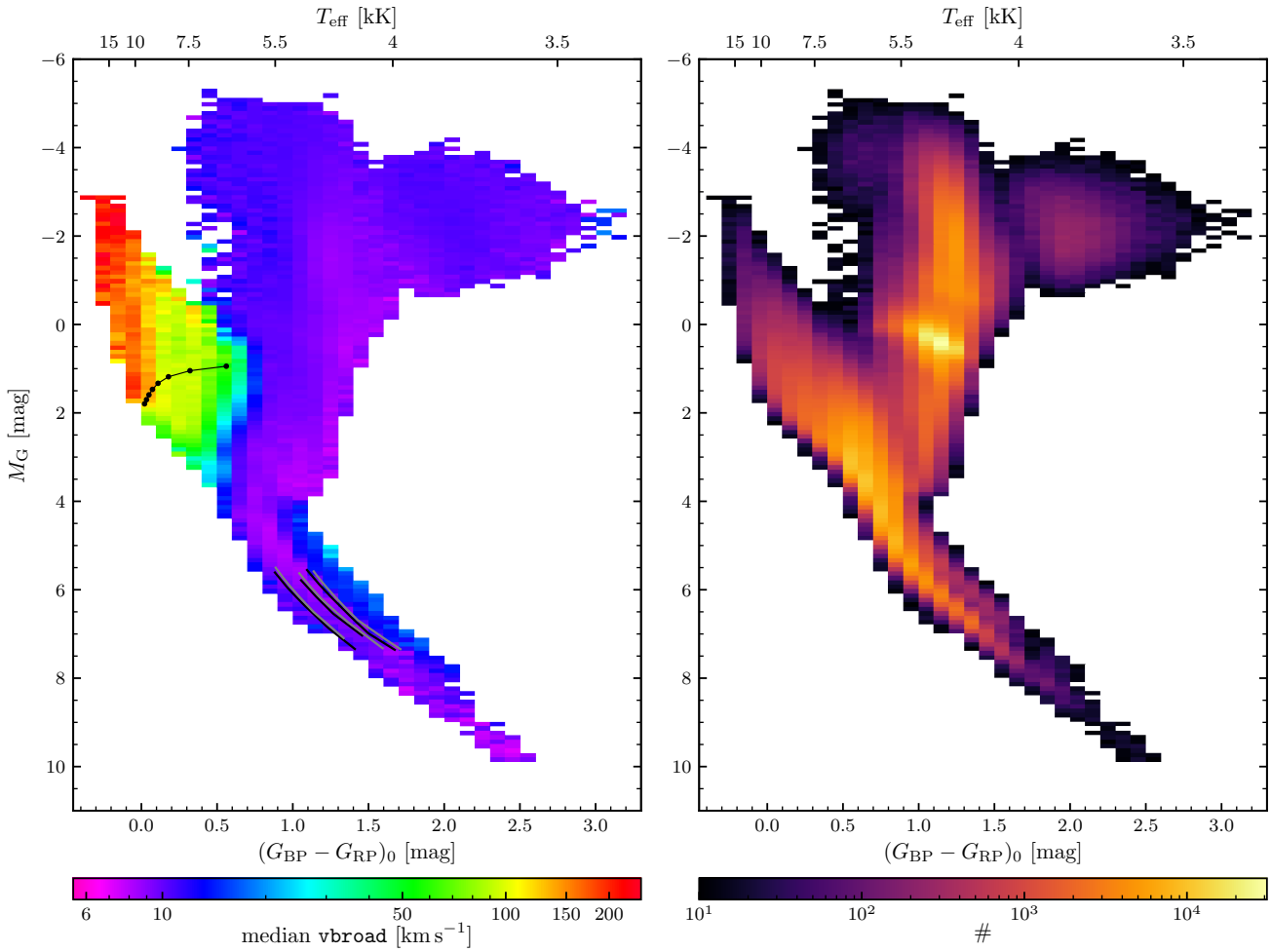

Fig. 16. Hertzsprung-Russell diagrams for a subsample of the *Gaia* DR3 `vbroad` catalogue (~1.8 million stars). The larger part of missing data is due to the lack of extinction parameters to correct for $M_{\rm G}$ and deredden $G_{\rm BP} - G_{\rm RP}$, which holds for about 43% of the sample. An additional cut is performed on the parallax quality ($\varpi/\sigma_\varpi > 10$) and removes 3.2% of the total sample. For hot stars, a selection is made on $G_{\rm RVS}$, which removes an additional 2.5% of the sample (see text). The binning size is 0.1 by 0.1 mag. Bins containing fewer than ten stars are discarded. *Left panel*: maps the median `vbroad` values (in logarithmic colour scale), and the *right panel* shows the density, in order to better associate the rotational velocity map to the corresponding structures in the HRD. To guide the eye, the upper x-axes show the approximate $T_{\rm eff}$ scale, calibrated as a function of $G_{\rm BP} - G_{\rm RP}$ using the photometric temperatures. The evolutionary track of a 2 $M_\odot$ star in the *left panel*, sampled each 162.5 Myr, illustrates the course from the ZAMS to the TAMS in the upper MS. In addition, three pairs of isochrones are superimposed on the lower MS for two different ages (1 Gyr in black and 10 Gyr in grey) and three different metallicities: [M/H] = −0.5, 0, and + 0.5, from left to right.

macroturbulence. However, $V_{\rm macro}$ is expected to vary in magnitude throughout the HRD. In late-type stars, its origin and impact is explained by surface convection and by 3D modelling (Asplund et al. 2000). At hotter temperatures, observations suggest that the origin of $V_{\rm macro}$ might be various competing phenomena: it can be related to line-profile variations (Aerts et al. 2009) due to surface inhomogeneity and pulsation, or to turbulent pressure (Grassitelli et al. 2015). Macroturbulence is usually expected to broaden the line shapes with a Gaussian-like kernel and requires data with a high S/N and high spectral resolution to be accurately distinguished from the rotational broadening. These conditions are clearly not met by the epoch *Gaia* DR3 RVS data. Accurate measurements based on 1D stellar atmosphere modelling show that its value increases with temperature and luminosity. In the $T_{\rm eff}$ range covered by the *Gaia* DR3 `vbroad` catalogue (i.e. $3500 \leq T_{\rm eff} \leq 14\,500$ K), macroturbulence is thought to increase with $T_{\rm eff}$, and with decreasing $\log g$ (Doyle et al. 2014). It has values of about 2 to 3.5 km s^{-1} at 5000 K, and 5 to 6.5 km s^{-1} at 6400 K. At the hottest edge, the line-broadening of B-type supergiants is typically dominated by $V_{\rm macro}$ with values higher than 25 km s^{-1} (Simón-Díaz et al. 2017). At lower luminosity, $V_{\rm macro}$ tends to be lower than $V \sin i$, but can still have values as high as ~60 km s^{-1}.

5.2. Effect of ignored binarity

A spectroscopically unresolved companion can also impact the measurements. According to Gao et al. (2014) and based on a sample of binaries with periods shorter than 1000 days, the value of the overall fraction of FGK binary systems in the Milky Way is expected to lie in the range of 0.30 to 0.56, depending on metallicity and on the data that were adopted to infer it. In solar-type stars and for close binaries (Moe et al. 2019), it was found to be anti-correlated with metallicity, varying from 0.53 to 0.24 for [Fe/H] = −3 to −0.2, respectively. Furthermore, this fraction of multiple systems is known to increase with mass and is observed to reach a value of 0.91 to 1 in O-type stars (Sana et al. 2014; we recall that the *Gaia* DR3 `vbroad` catalogue does not

include stars earlier than 14 500 K). During the processing and analysis of the RVS spectra, a significant effort was made to flag the double-lined spectroscopic binaries (Damerdji et al., in prep.; Katz et al. 2023), and to remove their median RV and vbroad estimates from the catalogue. As shown in Fig. 16, some binaries survived the post-processing cleaning. A counting of the sources in part of the single and binary star MS ($G_{BP} - G_{RP}$ ranging from 1.1 to 1.4) provides a fraction of 0.17 of MS candidate multiple stars that would still have a published vbroad estimate. A random visual inspection of the corresponding RVS spectra shows that while known spectroscopic binaries are found in the sample, most of them were not spectroscopically resolved. We may expect based on this hidden binarity a line profile and strength variability (e.g. panel f in Fig. B.1) that statistically produces a general overestimate of the line-broadening, as Fig. 16 suggests.

6. Conclusions

The *Gaia* DR3 catalogue provides the largest survey of line-broadening estimates down to magnitude 12, and from 3500 K to 14 500 K (Fig. 7). These estimates include all the line-broadening terms that are not taken into account by the synthetic spectra (e.g. $V \sin i$ and macroturbulence). As in other surveys (e.g. GALAH), we therefore called the measurement vbroad.

While our validation work generally shows that the measurements are fairly consistent with other surveys and compilations, it also recalls that the choice of the RVS wavelength domain was optimised to allow the RV measurement of most *Gaia* targets, but not for their accurate and non-biased determination of $V \sin i$. This is especially the case for stars hotter than 7500 K, when the features that dominate the spectrum are due to the intrinsically broad lines of the hydrogen Paschen series and of the Ca II triplet. By nature, these features are strongly blended, and their relative dependence on the astrophysical parameters may lead to template mismatches, to which the determination of vbroad is quite sensitive. As confirmed by the catalogue-to-catalogue comparisons, their impact was mitigated by the use of updated APs obtained for the hot stars during the RV processing (Blomme et al. 2023). However, at $T_{\rm eff} > 7500$ K, the dependence of the vbroad accuracy and precision on temperature and G_{RVS} remains complex and rapidly degrades above $G_{RVS} = 10$. The colour-magnitude diagram (Fig. 16) shows how the median vbroad varies in the HRD. While it reproduces the main feature expected due to magnetic braking in the cool stars around F5, it also highlights the potential effect of a mismatch due to metallicity between the observed spectrum and the template used to derive the value. Therefore, we recommend in general to remain cautious in the interpretation of the vbroad parameter values. To better help the catalogue user, we provide in Table 3 an estimate of the vbroad domains where both vbroad and its uncertainty are expected to be consistent with $V \sin i$.

During the processing of *Gaia* DR3, the vbroad results obtained by the method described in Sect. 2.1 were considered. More tests will be conducted during the preparation of the next data release in order to include the estimates from other algorithms (e.g. minimum distance method and use of the CCF width). The method presented in this paper uses the information integrated over the complete RVS domain (i.e. it produces one single CCF). It has obvious advantages for the fainter targets, but it is usually also dominated by the stronger and broader features, which are less sensitive to any additional line-broadening. With the tests we conduct to prepare *Gaia* DR4, we therefore determine the pertinence of isolating certain portions of the spectra that are more sensitive to the rotational broadening and of performing the measurement on coadded spectra.

Acknowledgements. We thank Dr Elena Pancino and the anonymous referee for carefully reading the manuscript and for providing us with constructive comments that helped to improve the paper. This work presents results from the European Space Agency (ESA) space mission *Gaia*. *Gaia* data are being processed by the *Gaia* Data Processing and Analysis Consortium (DPAC). Funding for the DPAC is provided by national institutions, in particular the institutions participating in the *Gaia* MultiLateral Agreement (MLA). The *Gaia* mission website is https://www.cosmos.esa.int/gaia. The *Gaia* archive website is https://archives.esac.esa.int/gaia. Full acknowledgements are given in Appendix A. This work has used the following software products: Matplotlib (Hunter 2007, https://matplotlib.org), SciPy (Virtanen et al. 2020, https://www.scipy.org), and NumPy (Harris et al. 2020, https://numpy.org). This research made use of the SIMBAD database, the Vizier catalogue access, and the cross-match services provided by CDS, Strasbourg, France.

References

Abt, H. A., & Morrell, N. I. 1995, ApJS, 99, 135
Abt, H. A., Levato, H., & Grosso, M. 2002, ApJ, 573, 359
Aerts, C., Puls, J., Godart, M., & Dupret, M. A. 2009, A&A, 508, 409
Allende Prieto, C., Beers, T. C., Wilhelm, R., et al. 2006, ApJ, 636, 804
Andrae, R., Fouesneau, M., Sordo, R., et al. 2023, A&A, 674, A27 (*Gaia* DR3 SI)
Asplund, M., Nordlund, Å., Trampedach, R., Allende Prieto, C., & Stein, R. F. 2000, A&A, 359, 729
Blomme, R., Edvardsson, B., Eriksson, K., et al. 2017, Gaia Data Processing and Analysis Consortium (DPAC) Technical Note GAIA-C6-TN-ROB-RHB-005. https://www.cosmos.esa.int/web/gaia/public-dpac-documents
Blomme, R., Frémat, Y., Sartoretti, P., et al. 2023, A&A, 674, A7 (*Gaia* DR3 SI)
Bressan, A., Marigo, P., Girardi, L., et al. 2012, MNRAS, 427, 127
Buder, S., Sharma, S., Kos, J., et al. 2021, MNRAS, 506, 150
Chen, Y.-P., Trager, S. C., Peletier, R. F., et al. 2014, A&A, 565, A117
Chen, Y., Bressan, A., Girardi, L., et al. 2015, MNRAS, 452, 1068
Cox, A. N. 2000, Allen's Astrophysical Quantities (New York, NY: Springer)
Creevey, O. L., Sordo, R., Pailler, F., et al. 2023, A&A, 674, A26 (*Gaia* DR3 SI)
Cropper, M., Katz, D., Sartoretti, P., et al. 2018, A&A, 616, A5
David, M., & Verschueren, W. 1995, A&AS, 111, 183
David, M., Blomme, R., Frémat, Y., et al. 2014, A&A, 562, A97
Doyle, A. P., Davies, G. R., Smalley, B., Chaplin, W. J., & Elsworth, Y. 2014, MNRAS, 444, 3592
Fouesneau, M., Frémat, Y., Andrae, R., et al. 2023, A&A, 674, A28 (*Gaia* DR3 SI)
Gao, S., Liu, C., Zhang, X., et al. 2014, ApJ, 788, L37
García Pérez, A. E., Allende Prieto, C., Holtzman, J. A., et al. 2016, AJ, 151, 144
Grassitelli, L., Fossati, L., Simón-Díáz, S., et al. 2015, ApJ, 808, L31
Głębocki, R., & Gnaciński, P. 2005, VizieR Online Data Catalog: III/244, [GG]
Harris, C. R., Millman, K. J., van der Walt, S. J., et al. 2020, Nature, 585, 357
Hunter, J. D. 2007, Comput. Sci. Eng., 9, 90
Jönsson, H., Holtzman, J. A., Allende Prieto, C., et al. 2020, AJ, 160, 120
Katz, D., Sartoretti, P., Cropper, M., et al. 2019, A&A, 622, A205
Katz, D., Sartoretti, P., Guerrier, A., et al. 2023, A&A, 674, A5 (*Gaia* DR3 SI)
Korn, A. J., Lobel, A., Kordopatis, G., et al. 2022, Gaia DR3 documentation Chapter 11.4.4: Atmospheric Parameters, https://gea.esac.esa.int/archive/documentation/GDR3/Data_analysis/chap_cu8par/sec_cu8par_validation/ssec_cu8par_qa_atmospheric-aps.html#SSS2
Kraft, R. P. 1967, ApJ, 150, 551
Marigo, P., Girardi, L., Bressan, A., et al. 2017, ApJ, 835, 77
Moe, M., Kratter, K. M., & Badenes, C. 2019, ApJ, 875, 61
Munari, U. 1999, Baltic Astron., 8, 73
Nordström, B., Mayor, M., Andersen, J., et al. 2004, A&A, 418, 989
Pastorelli, G., Marigo, P., Girardi, L., et al. 2019, MNRAS, 485, 5666
Pastorelli, G., Marigo, P., Girardi, L., et al. 2020, MNRAS, 498, 3283
Pineau, F. X., Boch, T., Derrière, S., & Schaaff, A. 2020, in Astronomical Data Analysis Software and Systems XXVII, eds. P. Ballester, J. Ibsen, M. Solar, & K. Shortridge, ASP Conf. Ser., 522, 125
Piskunov, N., & Valenti, J. A. 2017, A&A, 597, A16
Recio-Blanco, A., de Laverny, P., Palicio, P. A., et al. 2023, A&A, 674, A29 (*Gaia* DR3 SI)
Riello, M., De Angeli, F., Evans, D. W., et al. 2021, A&A, 649, A3
Royer, F. 2014, in Putting A Stars into Context: Evolution, Environment, andRelated Stars, eds. G. Mathys, E. R. Griffin, O. Kochukhov, R. Monier, & G. M. Wahlgren, 256
Sana, H., Bouquin, J.-B. L., Lacour, S., et al. 2014, ApJS, 215, 15

Sartoretti, P., Katz, D., Cropper, M., et al. 2018, A&A, 616, A6
Sartoretti, P., Blomme, R., David, M., & Seabroke, G. 2022, Gaia DR3 documentation Chapter 6: Spectroscopy, https://gea.esac.esa.int/archive/documentation/GDR3/Data_processing/chap_cu6spe/
Sartoretti, P., Marchal, O., Babusiaux, C., et al. 2023, A&A, 674, A6 (*Gaia* DR3 SI)
Siebert, A., Williams, M. E. K., Siviero, A., et al. 2011, AJ, 141, 187
Simón-Díaz, S., Godart, M., Castro, N., et al. 2017, A&A, 597, A22
Soderblom, D. R., Pendleton, J., & Pallavicini, R. 1989, AJ, 97, 539
Steinmetz, M., Guiglion, G., McMillan, P. J., et al. 2020, AJ, 160, 83
Tang, J., Bressan, A., Rosenfield, P., et al. 2014, MNRAS, 445, 4287
Uesugi, A., & Fukuda, I. 1982, Catalogue of Stellar Rotational Velocities (revised) (Kyoto: University of Kyoto)
Virtanen, P., Gommers, R., Oliphant, T. E., et al. 2020, Nat. Methods, 17, 261
Xiang, M., Rix, H.-W., Ting, Y.-S., et al. 2022, A&A, 662, A66
Zwitter, T., Siebert, A., Munari, U., et al. 2008, AJ, 136, 421

[1] Royal Observatory of Belgium, Avenue circulaire 3, 1180 Bruxelles, Belgium
[2] GEPI, Observatoire de Paris, Université PSL, CNRS, 5 Place Jules Janssen, 92190 Meudon, France
[3] Observatoire astronomique de Strasbourg, Université de Strasbourg, CNRS, 11 rue de l'Université, 67000 Strasbourg, France
[4] CNES Centre Spatial de Toulouse, 18 avenue Edouard Belin, 31401 Toulouse Cedex 9, France
[5] Mullard Space Science Laboratory, University College London, Holmbury St Mary, Dorking, Surrey RH5 6NT, UK
[6] Université Côte d'Azur, Observatoire de la Côte d'Azur, CNRS, Laboratoire Lagrange, Boulevard de l'Observatoire, CS 34229, 06304 Nice, France
[7] CRAAG – Centre de Recherche en Astronomie, Astrophysique et Géophysique, Route de l'Observatoire, Bp 63 Bouzareah, 16340 Alger, Algeria
[8] Institut d'Astrophysique et de Géophysique, Université de Liège, 19c, Allée du 6 Août, 4000 Liège, Belgium
[9] Centro de Astronomía, Universidad de Antofagasta, Avda. U. de Antofagasta, 02800 Antofagasta, Chile
[10] Universiteit Antwerpen, Onderzoeksgroep Toegepaste Wiskunde, Middelheimlaan 1, 2020 Antwerpen, Belgium
[11] F.R.S.-FNRS, Rue d'Egmont 5, 1000 Brussels, Belgium
[12] Leibniz Institute for Astrophysics Potsdam (AIP), An der Sternwarte 16, 14482 Potsdam, Germany
[13] Laboratoire Univers et Particules de Montpellier, Université Montpellier, CNRS, Place Eugène Bataillon, CC72, 34095 Montpellier Cedex 05, France
[14] Astronomical Institute, Faculty of Mathematics and Physics, Charles University, V Holešovičkách 2, 180 00 Prague, Czech Republic
[15] Laboratoire d'astrophysique de Bordeaux, Université de Bordeaux, CNRS, B18N, allée Geoffroy Saint-Hilaire, 33615 Pessac, France
[16] Sorbonne Université CNRS, UMR 7095, Institut d'Astrophysique de Paris, 75014 Paris, France
[17] Faculty of Mathematics and Physics, University of Ljubljana, Jadranska ulica 19, 1000 Ljubljana, Slovenia
[18] Institute for Computational Cosmology, Department of Physics, Durham University, Durham DH1 3LE, UK
[19] European Southern Observatory, Karl-Schwarzschild-Str. 2, 85748 Garching-bei-München, Germany

Appendix A: Full aknowledgements

This work presents results from the European Space Agency (ESA) space mission *Gaia*. *Gaia* data are being processed by the *Gaia* Data Processing and Analysis Consortium (DPAC). Funding for the DPAC is provided by national institutions, in particular the institutions participating in the *Gaia* MultiLateral Agreement (MLA). The *Gaia* mission website is https://www.cosmos.esa.int/gaia. The *Gaia* archive website is https://archives.esac.esa.int/gaia.

The *Gaia* mission and data processing have financially been supported by, in alphabetical order by country:

- the Algerian Centre de Recherche en Astronomie, Astrophysique et Géophysique of Bouzareah Observatory;
- the Austrian Fonds zur Förderung der wissenschaftlichen Forschung (FWF) Hertha Firnberg Programme through grants T359, P20046, and P23737;
- the BELgian federal Science Policy Office (BELSPO) through various PROgramme de Développement d'Expériences scientifiques (PRODEX) grants and the Polish Academy of Sciences - Fonds Wetenschappelijk Onderzoek through grant VS.091.16N, and the Fonds de la Recherche Scientifique (FNRS), and the Research Council of Katholieke Universiteit (KU) Leuven through grant C16/18/005 (Pushing AsteRoseismology to the next level with TESS, GaiA, and the Sloan DIgital Sky SurvEy – PARADISE);
- the Brazil-France exchange programmes Fundação de Amparo à Pesquisa do Estado de São Paulo (FAPESP) and Coordenação de Aperfeicoamento de Pessoal de Nível Superior (CAPES) - Comité Français d'Evaluation de la Coopération Universitaire et Scientifique avec le Brésil (COFECUB);
- the Chilean Agencia Nacional de Investigación y Desarrollo (ANID) through Fondo Nacional de Desarrollo Científico y Tecnológico (FONDECYT) Regular Project 1210992 (L. Chemin);
- the National Natural Science Foundation of China (NSFC) through grants 11573054, 11703065, and 12173069, the China Scholarship Council through grant 201806040200, and the Natural Science Foundation of Shanghai through grant 21ZR1474100;
- the Tenure Track Pilot Programme of the Croatian Science Foundation and the École Polytechnique Fédérale de Lausanne and the project TTP-2018-07-1171 'Mining the Variable Sky', with the funds of the Croatian-Swiss Research Programme;
- the Czech-Republic Ministry of Education, Youth, and Sports through grant LG 15010 and INTER-EXCELLENCE grant LTAUSA18093, and the Czech Space Office through ESA PECS contract 98058;
- the Danish Ministry of Science;
- the Estonian Ministry of Education and Research through grant IUT40-1;
- the European Commission's Sixth Framework Programme through the European Leadership in Space Astrometry (ELSA) Marie Curie Research Training Network (MRTN-CT-2006-033481), through Marie Curie project PIOF-GA-2009-255267 (Space AsteroSeismology & RR Lyrae stars, SAS-RRL), and through a Marie Curie Transfer-of-Knowledge (ToK) fellowship (MTKD-CT-2004-014188); the European Commission's Seventh Framework Programme through grant FP7-606740 (FP7-SPACE-2013-1) for the *Gaia* European Network for Improved data User Services (GENIUS) and through grant 264895 for the *Gaia* Research for European Astronomy Training (GREAT-ITN) network;
- the European Cooperation in Science and Technology (COST) through COST Action CA18104 'Revealing the Milky Way with *Gaia* (MW-Gaia)';
- the European Research Council (ERC) through grants 320360, 647208, and 834148 and through the European Union's Horizon 2020 research and innovation and excellent science programmes through Marie Skłodowska-Curie grant 745617 (Our Galaxy at full HD – Gal-HD) and 895174 (The build-up and fate of self-gravitating systems in the Universe) as well as grants 687378 (Small Bodies: Near and Far), 682115 (Using the Magellanic Clouds to Understand the Interaction of Galaxies), 695099 (A sub-percent distance scale from binaries and Cepheids – CepBin), 716155 (Structured ACCREtion Disks – SACCRED), 951549 (Sub-percent calibration of the extragalactic distance scale in the era of big surveys – UniverScale), and 101004214 (Innovative Scientific Data Exploration and Exploitation Applications for Space Sciences – EXPLORE);
- the European Science Foundation (ESF), in the framework of the *Gaia* Research for European Astronomy Training Research Network Programme (GREAT-ESF);
- the European Space Agency (ESA) in the framework of the *Gaia* project, through the Plan for European Cooperating States (PECS) programme through contracts C98090 and 4000106398/12/NL/KML for Hungary, through contract 4000115263/15/NL/IB for Germany, and through PROgramme de Développement d'Expériences scientifiques (PRODEX) grant 4000127986 for Slovenia;
- the Academy of Finland through grants 299543, 307157, 325805, 328654, 336546, and 345115 and the Magnus Ehrnrooth Foundation;
- the French Centre National d'Études Spatiales (CNES), the Agence Nationale de la Recherche (ANR) through grant ANR-10-IDEX-0001-02 for the 'Investissements d'avenir' programme, through grant ANR-15-CE31-0007 for project 'Modelling the Milky Way in the *Gaia* era' (MOD4Gaia), through grant ANR-14-CE33-0014-01 for project 'The Milky Way disc formation in the *Gaia* era' (ARCHEOGAL), through grant ANR-15-CE31-0012-01 for project 'Unlocking the potential of Cepheids as primary distance calibrators' (UnlockCepheids), through grant ANR-19-CE31-0017 for project 'Secular evolution of galaxies' (SEGAL), and through grant ANR-18-CE31-0006 for project 'Galactic Dark Matter' (GaDaMa), the Centre National de la Recherche Scientifique (CNRS) and its SNO *Gaia* of the Institut des Sciences de l'Univers (INSU), its Programmes Nationaux: Cosmologie et Galaxies (PNCG), Gravitation Références Astronomie Métrologie (PNGRAM), Planétologie (PNP), Physique et Chimie du Milieu Interstellaire (PCMI), and Physique Stellaire (PNPS), the 'Action Fédératrice *Gaia*' of the Observatoire de Paris, the Région de Franche-Comté, the Institut National Polytechnique (INP) and the Institut National de Physique nucléaire et de Physique des Particules (IN2P3) co-funded by CNES;
- the German Aerospace Agency (Deutsches Zentrum für Luft- und Raumfahrt e.V., DLR) through grants 50QG0501, 50QG0601, 50QG0602, 50QG0701, 50QG0901, 50QG 1001, 50QG1101, 50QG1401, 50QG1402, 50QG1403, 50QG1404, 50QG1904, 50QG2101, 50QG2102, and 50QG 2202, and the Centre for Information Services and High Performance Computing (ZIH) at the Technische Universität Dresden for generous allocations of computer time;

– the Hungarian Academy of Sciences through the Lendület Programme grants LP2014-17 and LP2018-7 and the Hungarian National Research, Development, and Innovation Office (NKFIH) through grant KKP-137523 ('SeismoLab');
– the Science Foundation Ireland (SFI) through a Royal Society - SFI University Research Fellowship (M. Fraser);
– the Israel Ministry of Science and Technology through grant 3-18143 and the Tel Aviv University Center for Artificial Intelligence and Data Science (TAD) through a grant;
– the Agenzia Spaziale Italiana (ASI) through contracts I/037/08/0, I/058/10/0, 2014-025-R.0, 2014-025-R.1.2015, and 2018-24-HH.0 to the Italian Istituto Nazionale di Astrofisica (INAF), contract 2014-049-R.0/1/2 to INAF for the Space Science Data Centre (SSDC, formerly known as the ASI Science Data Center, ASDC), contracts I/008/10/0, 2013/030/I.0, 2013-030-I.0.1-2015, and 2016-17-I.0 to the Aerospace Logistics Technology Engineering Company (ALTEC S.p.A.), INAF, and the Italian Ministry of Education, University, and Research (Ministero dell'Istruzione, dell'Università e della Ricerca) through the Premiale project 'MIning The Cosmos Big Data and Innovative Italian Technology for Frontier Astrophysics and Cosmology' (MITiC);
– the Netherlands Organisation for Scientific Research (NWO) through grant NWO-M-614.061.414, through a VICI grant (A. Helmi), and through a Spinoza prize (A. Helmi), and the Netherlands Research School for Astronomy (NOVA);
– the Polish National Science Centre through HARMONIA grant 2018/30/M/ST9/00311 and DAINA grant 2017/27/L/ST9/03221 and the Ministry of Science and Higher Education (MNiSW) through grant DIR/WK/2018/12;
– the Portuguese Fundação para a Ciência e a Tecnologia (FCT) through national funds, grants SFRH/BD/128840/2017 and PTDC/FIS-AST/30389/2017, and work contract DL 57/2016/CP1364/CT0006, the Fundo Europeu de Desenvolvimento Regional (FEDER) through grant POCI-01-0145-FEDER-030389 and its Programa Operacional Competitividade e Internacionalização (COMPETE2020) through grants UIDB/04434/2020 and UIDP/04434/2020, and the Strategic Programme UIDB/00099/2020 for the Centro de Astrofísica e Gravitação (CENTRA);
– the Slovenian Research Agency through grant P1-0188;
– the Spanish Ministry of Economy (MINECO/FEDER, UE), the Spanish Ministry of Science and Innovation (MICIN), the Spanish Ministry of Education, Culture, and Sports, and the Spanish Government through grants BES-2016-078499, BES-2017-083126, BES-C-2017-0085, ESP2016-80079-C2-1-R, ESP2016-80079-C2-2-R, FPU16/03827, PDC2021-121059-C22, RTI2018-095076-B-C22, and TIN2015-65316-P ('Computación de Altas Prestaciones VII'), the Juan de la Cierva Incorporación Programme (FJCI-2015-2671 and IJC2019-04862-I for F. Anders), the Severo Ochoa Centre of Excellence Programme (SEV2015-0493), and MICIN/AEI/10.13039/501100011033 (and the European Union through European Regional Development Fund 'A way of making Europe') through grant RTI2018-095076-B-C21, the Institute of Cosmos Sciences University of Barcelona (ICCUB, Unidad de Excelencia 'María de Maeztu') through grant CEX2019-000918-M, the University of Barcelona's official doctoral programme for the development of an R+D+i project through an Ajuts de Personal Investigador en Formació (APIF) grant, the Spanish Virtual Observatory through project AyA2017-84089, the Galician Regional Government, Xunta de Galicia, through grants ED431B-2021/36, ED481A-2019/155, and ED481A-2021/296, the Centro de Investigación en Tecnologías de la Información y las Comunicaciones (CITIC), funded by the Xunta de Galicia and the European Union (European Regional Development Fund – Galicia 2014-2020 Programme), through grant ED431G-2019/01, the Red Española de Supercomputación (RES) computer resources at MareNostrum, the Barcelona Supercomputing Centre - Centro Nacional de Supercomputación (BSC-CNS) through activities AECT-2017-2-0002, AECT-2017-3-0006, AECT-2018-1-0017, AECT-2018-2-0013, AECT-2018-3-0011, AECT-2019-1-0010, AECT-2019-2-0014, AECT-2019-3-0003, AECT-2020-1-0004, and DATA-2020-1-0010, the Departament d'Innovació, Universitats i Empresa de la Generalitat de Catalunya through grant 2014-SGR-1051 for project 'Models de Programació i Entorns d'Execució Parallels' (MPEXPAR), and Ramon y Cajal Fellowship RYC2018-025968-I funded by MICIN/AEI/10.13039/501100011033 and the European Science Foundation ('Investing in your future');
– the Swedish National Space Agency (SNSA/Rymdstyrelsen);
– the Swiss State Secretariat for Education, Research, and Innovation through the Swiss Activités Nationales Complémentaires and the Swiss National Science Foundation through an Eccellenza Professorial Fellowship (award PCEFP2_194638 for R. Anderson);
– the United Kingdom Particle Physics and Astronomy Research Council (PPARC), the United Kingdom Science and Technology Facilities Council (STFC), and the United Kingdom Space Agency (UKSA) through the following grants to the University of Bristol, the University of Cambridge, the University of Edinburgh, the University of Leicester, the Mullard Space Sciences Laboratory of University College London, and the United Kingdom Rutherford Appleton Laboratory (RAL): PP/D006511/1, PP/D006546/1, PP/D006570/1, ST/I000852/1, ST/J005045/1, ST/K00056X/1, ST/K000209/1, ST/K000756/1, ST/L006561/1, ST/N000595/1, ST/N000641/1, ST/N000978/1, ST/N001117/1, ST/S000089/1, ST/S000976/1, ST/S000984/1, ST/S001123/1, ST/S001948/1, ST/S001980/1, ST/S002103/1, ST/V000969/1, ST/W002469/1, ST/W002493/1, ST/W002671/1, ST/W002809/1, and EP/V520342/1.

The GBOT programme uses observations collected at (i) the European Organisation for Astronomical Research in the Southern Hemisphere (ESO) with the VLT Survey Telescope (VST), under ESO programmes 092.B-0165, 093.B-0236, 094.B-0181, 095.B-0046, 096.B-0162, 097.B-0304, 098.B-0030, 099.B-0034, 0100.B-0131, 0101.B-0156, 0102.B-0174, and 0103.B-0165; and (ii) the Liverpool Telescope, which is operated on the island of La Palma by Liverpool John Moores University in the Spanish Observatorio del Roque de los Muchachos of the Instituto de Astrofísica de Canarias with financial support from the United Kingdom Science and Technology Facilities Council, and (iii) telescopes of the Las Cumbres Observatory Global Telescope Network.

Appendix B: Selected RVS spectra

We show in Fig. B.1 a selection of spectra with different values of $G_{\rm RVS}$, $T_{\rm eff}$, $\log g$, [Fe/H], and `vbroad` (see also Table B.1). From cool to hotter targets, panels a) to d) show the variation in relative strength of the Ca II triplet and hydrogen Paschen lines with effective temperature. Above $G_{\rm RVS} = 10$, the weakest spectral lines, which usually are more sensitive to `vbroad`, are

disappearing rapidly in the noise, while in the hottest star (panel d), the main features are the broad lines of the Paschen series. These data are transit spectra, which are not part of the *Gaia* DR3 release.

The pipeline we used to derive the radial velocities is able to flag the most obvious cases of emission-line stars and spectroscopic binaries. However, spectra belonging to targets exhibiting signatures of chromospheric activity (see panel e and its inset) that could not be automatically identified still have published `vbroad` estimates. The same is true for a fraction of undetected binaries (e.g. those that in most transits are not spectroscopically resolved). One example is presented in panel f) for a target located in the colour magnitude diagram of Fig. 16 on the binary MS. Line-core emission in the spectra of active stars as well as line-profile asymmetry due to binarity are expected to bias the `vbroad` determinations.

Table B.1. Description of the template spectra shown in each panel of Fig. B.1.

	Gaia DR3 ID	$G_{\rm RVS}$	`rv_template_` `teff` [K]	`logg`	`fe_h`	`vbroad` [km s^{-1}]
a)	4281604312712348416	5.30	3700	1.00	+0.25	9
b)	5500304413985680768	6.78	6500	4.50	−0.25	85
c)	154688508503362560	9.33	8000	4.50	+0.25	54
d)	1982777497654568576	8.66	14000	4.00	+0.25	300
e)	68303487680516224	10.40	5500	4.50	+0.25	73
f)	1400996792695779328	8.88	4750	5.00	+0.00	12

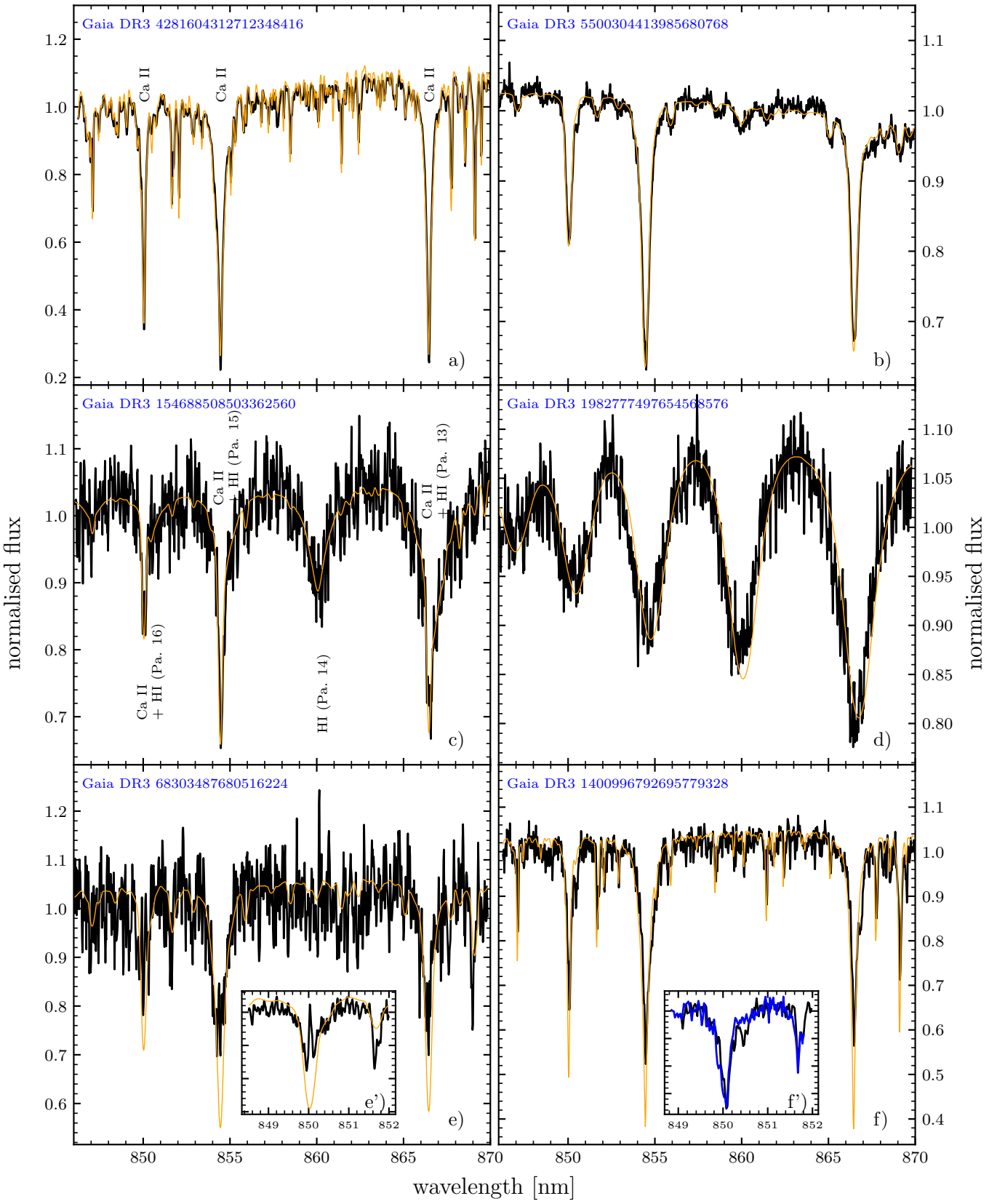

Fig. B.1. Examples of RVS spectra used to derive the `vbroad` parameter. Transit spectra (black curve) are compared to the template spectrum used to measure `vbroad` (orange curve) and broadened to the published estimate. The inset of panel e) zooms in on the corresponding **multiple transit combined** spectrum (i.e. black curve in subpanel e') to show the signature of chromospheric activity. The inset of panel f) compares two transit spectra (black and blue) of the same target. The target IDs are given in blue in the upper left corner of the panels, and the $G_{\rm RVS}$ magnitude and astrophysical parameters considered to select and broaden the template spectra (orange) are given in Table B.1. The spectra we used to make these plots are not part of the *Gaia* DR3 release.